Neuron
Article

Entrainment of Neocortical Neurons and Gamma Oscillations by the Hippocampal Theta Rhythm

Anton Sirota,[1] Sean Montgomery,[1] Shigeyoshi Fujisawa,[1] Yoshikazu Isomura,[1,2] Michael Zugaro,[1,3] and György Buzsáki[1,*]
[1]Center for Molecular and Behavioral Neuroscience, Rutgers, The State University of New Jersey, 197 University Avenue, Newark, NJ 07102, USA
[2]Present address: Neural Circuit Theory, RIKEN Brain Science Institute, 2-1 Hirosawa, Wako, Saitama 351-0198, Japan
[3]Present address: CNRS - Collège de France, LPPA, UMR 7152, 11, place Marcelin Berthelot, 75005 Paris, France
*Correspondence: buzsaki@axon.rutgers.edu
DOI 10.1016/j.neuron.2008.09.014

SUMMARY

Although it has been tacitly assumed that the hippocampus exerts an influence on neocortical networks, the mechanisms of this process are not well understood. We examined whether and how hippocampal theta oscillations affect neocortical assembly patterns by recording populations of single cells and transient gamma oscillations in multiple cortical regions, including the somatosensory area and prefrontal cortex in behaving rats and mice. Laminar analysis of neocortical gamma bursts revealed multiple gamma oscillators of varying frequency and location, which were spatially confined and synchronized local groups of neurons. A significant fraction of putative pyramidal cells and interneurons as well as localized gamma oscillations in all recorded neocortical areas were phase biased by the hippocampal theta rhythm. We hypothesize that temporal coordination of neocortical gamma oscillators by hippocampal theta is a mechanism by which information contained in spatially widespread neocortical assemblies can be synchronously transferred to the associative networks of the hippocampus.

INTRODUCTION

An essential aspect of cortical operation is that the results of local computations are integrated globally. Although the mechanisms of such local-global interactions are not well understood (Buzsáki, 2006; Dehaene et al., 2003; Engel et al., 2001; Varela et al., 2001), network oscillations have been assumed to play a critical role (Destexhe and Sejnowski, 2001; Engel et al., 2001). A general feature of cortical oscillations is that slow rhythms engage large areas and effectively modulate the more localized and shorter-lived fast oscillations (Bragin et al., 1995; Chrobak and Buzsáki, 1998a; Lakatos et al., 2005). Integration of information between different structures, such as the hippocampus and neocortex, is a special case of global coordination.

In waking cortical networks, local cell assembly organization is reflected in the occurrence of gamma oscillations (Gray and Singer, 1989; Harris et al., 2003). In the hippocampus, "activation" state is reflected by highly synchronous theta frequency oscillations (Buzsáki, 2002; Grastyán et al., 1959; Green and Arduni, 1954; Jouvet, 1969; Vanderwolf, 1969), which has been hypothesized to serve as a temporal organizer for a variety of functions (Bland, 1986; O'Keefe and Burgess, 2005). Theta-modulated cells have been found in the entorhinal cortex (Alonso and Garcia-Austt, 1987; Chrobak and Buzsáki, 1998b), perirhinal cortex (Muir and Bilkey, 1998), cingulate cortex (Colom et al., 1988; Holsheimer, 1982; Leung and Borst, 1987), prefrontal cortex (Hyman et al., 2005; Jones and Wilson, 2005; Siapas et al., 2005), amygdala (Collins et al., 1999; Paré and Gaudreau, 1996), anterior thalamus (Vertes et al., 2001), mammillary bodies, the supramammillary nucleus (Kocsis and Vertes, 1994), and the subiculum (Anderson and O'Mara, 2003). In addition, the rhythmic synchronous output of the hippocampus has been suggested to time the initiation of voluntary movements (Berg et al., 2006; Buño and Velluti, 1977; Macrides et al., 1982; Semba and Komisaruk, 1978) and gate sensory information (cf. Bland, 1986). Mainly on the basis of these behavioral results, the influence of hippocampal theta oscillations on neurons outside the limbic areas has been repeatedly conjectured (Bland, 1986; Buño and Velluti, 1977; Miller, 1991; Semba and Komisaruk, 1978), but experimental evidence to support this function is lacking. Phase modulation is a potential mechanism by which the hippocampus can coordinate disparate neocortical cell assemblies. To test this hypothesis and expand on previous works (Hyman et al., 2005; Jones and Wilson, 2005; Siapas et al., 2005), we recorded unit activity and local field potentials (LFP) from multiple neocortical regions, including primary sensory areas and the medial prefrontal cortex (PFC), along with hippocampal activity in rats and mice. We report here that a significant fraction of neurons in all recorded neocortical areas and locally emerging gamma oscillations are phase modulated by the hippocampal theta rhythm.

RESULTS

To investigate the effect of hippocampal theta oscillations on neocortical networks we recorded multiple single units and LFP in the associative and primary somatosensory (Figure 1A,

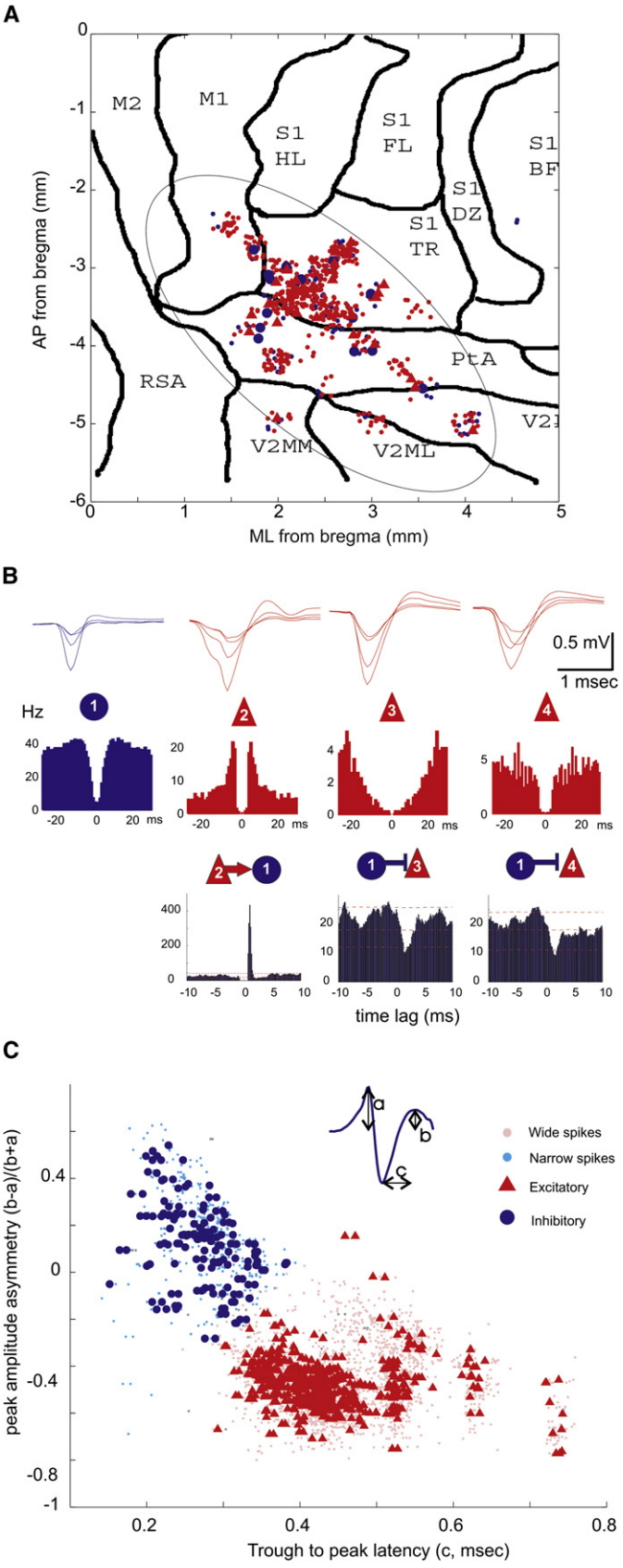

Figure 1. Separation of Putative Neocortical Interneurons and Pyramidal Cells

(A) Topographic distribution of putative pyramidal cells (red dots, triangles) and interneurons (small and larger blue dots) recorded from the parietal cortical area in all animals. Each symbol corresponds to a neuron (n = 767 from 24 rats), the position of which was inferred from implantation coordinates of the electrodes on a flattened cortical map. M1, M2, motor cortex; S1, primary somatosensory cortex; HL, hindlimb; FL, forelimb; BF, barrel field; TR, trunk; PtA, posterior associative area; V2MM, V2ML, secondary visual cortex; RSA, retrosplenial cortex.

(B) Average wide band-recorded waveforms (1 Hz-5 kHz; upper row) and autocorrelograms (middle row) of four example units. Superimposed traces were recorded by the four tetrode sites. Bottom row, short-latency monosynaptic interactions between neuron pairs, as revealed from the crosscorrelograms. Neuron 2 excites neuron 1 (recorded on the same electrode), which in turn, inhibits neurons 3 and 4 (on a different electrode). Lines indicate mean and 1% and 99% global confidence intervals.

(C) Neurons were clustered according to waveform asymmetry and mean filtered spike width (see inset; 0.8–5 kHz). Each symbol corresponds to an isolated unit (n = 2716, including neurons recorded from the medial prefrontal cortex, mPFC). Putative excitatory and inhibitory neurons form separate clusters. Circles/triangles in (A) and (C) correspond to inhibitory and excitatory neurons identified by monosynaptic interactions (as in [B]; Barthó et al., 2004).

referred to here as "parietal") areas or the anterior cingulate and prelimbic divisions of the medial prefrontal cortex (PFC) in 28 rats and 11 mice during task performance on an elevated maze and/or REM sleep. The reference theta oscillation signal was always derived from the CA1 pyramidal layer of the dorsal hippocampus (see Figure S1 available online).

Segregation of Principal Cells and Inhibitory Interneurons

Network activity in the cortex is organized by the interplay of various classes of principal cells and inhibitory interneurons (Markram, 2006; Somogyi and Klausberger, 2005). Since these two major classes of neurons have different firing rates, circuit and resonant properties and contribute differentially to cortical operations (Beierlein et al., 2000; Freund and Buzsáki, 1996; Markram, 2006), experimental identification, and separation of excitatory principal cells and inhibitory neurons are important for studying the effects of afferent signals on neocortical activity. Simultaneous recording of multiple single units in a small neocortical volume allowed us to identify putative principal cells and inhibitory interneurons (Figures 1B and 1C; Barthó et al., 2004; Constantinidis and Goldman-Rakic, 2002; Tierney et al., 2004; see Supplemental Data). The majority of the recorded neocortical units were classified as putative pyramidal cells (n = 2297, 85% in rats, n = 72, 84% mice) and the minority as putative interneurons (n = 343, 13% in rats; n = 14, 16% in mice).

Hippocampal Theta Phase-Locking of Neocortical Neurons

Several statistical methods were used to quantify the significance and magnitude of theta phase-locking of neocortical cells (Figures 2A–2D). Using Rayleigh tests (Figures 2E and 2F; α = 0.05) we found that the percentage of significantly modulated interneurons was higher than that of pyramidal cells in both parietal (32% versus 11%, respectively) and prefrontal cortices (46% versus 28%, respectively). The percentage of both cell types with significant theta phase-locking was significantly higher in PFC than in the parietal area (Figures 2E and 2F), but the fractions of significantly modulated neurons within the parietal subregions were similar (interneurons/pyramidal cells; S1: 33%/10%; posterior associative area [PtA]: 27%/11%). In contrast, the depth of theta modulation (von Mises concentration coefficient) of pyramidal cells was consistently higher than that of the interneurons (Figure S2). Additional analyses, including nonparametric tests, fit of a mixture model and spectral analysis, aimed to control for the assumptions of the Rayleigh test and gave comparable results (Supplemental Data; Figures S2 and S3). The preferred phases of significantly modulated neurons were similarly and broadly distributed for both interneurons and pyramidal cells, with highest density corresponding to the peak/descending phase of the CA1 theta cycle (Figures 2G and 2H).

Theta phase-locking of neocortical neurons occurred during both running on the track and REM sleep. Neurons could be significantly phase locked to theta in either one or both of these theta-associated states (Figures 2I–2L). In the subset of significantly modulated neurons that were recorded in both states the preferred phase of theta modulation was correlated across states (Figure 2L; $R_{circular}$ = 0.42). On average, the preferred phase of the population was significantly delayed during running compared to during REM in PFC, but not in the parietal cortex ($\sim 75^{\circ}$; circular anova, $p < 10^{-5}$ and $p > 0.3$, respectively; Figures 2K and 2L). Comparable results were obtained in mice (Figure S4). Approximately 60% of putative interneurons (of n = 14 total) and 35% of pyramidal neurons (of n = 72) were significantly (α = 0.05) modulated, with similar theta phase preferences across the population. These findings in rats and mice show that hippocampal theta oscillations impose a detectable phase-modulatory effect on the firing rate of neocortical neurons.

Locally Generated Neocortical Gamma Oscillations

Before examining the impact of theta phase on gamma oscillations, we investigated the local origin of gamma activity in the neocortex. First, we estimated the coherence between spike trains of pairs of neurons with sufficiently high firing rates (>5Hz). In a fraction of them (n = 123 pairs, 15% ± 10% of all pairs) significant coherence peaks between 30 and 140 Hz were found (Figure S5). Next, we computed the coherence between unit firing and the LFP recorded at multiple sites of the silicon probe (Figure 3A). Spikes were locked most coherently in a narrow band of a particular gamma frequency to the LFP in a localized cortical volume (Figures 3B–3D, 3F, and S6A–S6C). Spike-LFP coherence in the gamma band was in general, though not always, highest around the soma of the respective unit and decreased with distance (Figures 3D and 3E). Most neurons were phase-locked to the troughs of LFP gamma cycles (Figure 3G). In a related approach, we calculated average spectral power in short (50–100 ms) epochs temporally surrounding the action potentials of single neurons. Similar to coherence analysis, these "spike-triggered" spectra showed strong correlation between the firing of a subset of neurons and the LFP power within specific narrow ranges of gamma frequency oscillations in localized neocortical areas (Figures 3H, 3I, and S6D–S6I). Analysis of spectra at various time lags from the triggering spike showed that increases of the space-frequency localized power were transient, reaching maximum within 0–100 ms from the reference spike (Figure S6). Some data sets contained simultaneously recorded neurons that were phase-locked or correlated with gamma oscillations, which were localized at the same location (putative layer and/or column) and/or frequency (e.g., Figures 3C, 3D, 3H, and 3I), indicating that gamma oscillations with particular localization and/or frequency are associated with the activity of unique groups of neurons.

Synchronization of pools of neurons was tentatively associated with transient increases of LFP power at specific locations and narrow gamma frequency bands. Because of volume conduction and the linear summation of different transient gamma oscillations with variable amplitudes and frequencies continuous summation of spectral power in the gamma band may not yield reliable results. Therefore, we devised two alternative approaches. The first approach is based on the monotonous decay of power away from gamma sources. Exploiting our multiple site recordings, a subset of well isolated gamma bursts were detected as local maxima of the spectral power in time, space, and frequency, and the detected events tended to cluster (e.g., Figure 4). The second approach for the detection of gamma

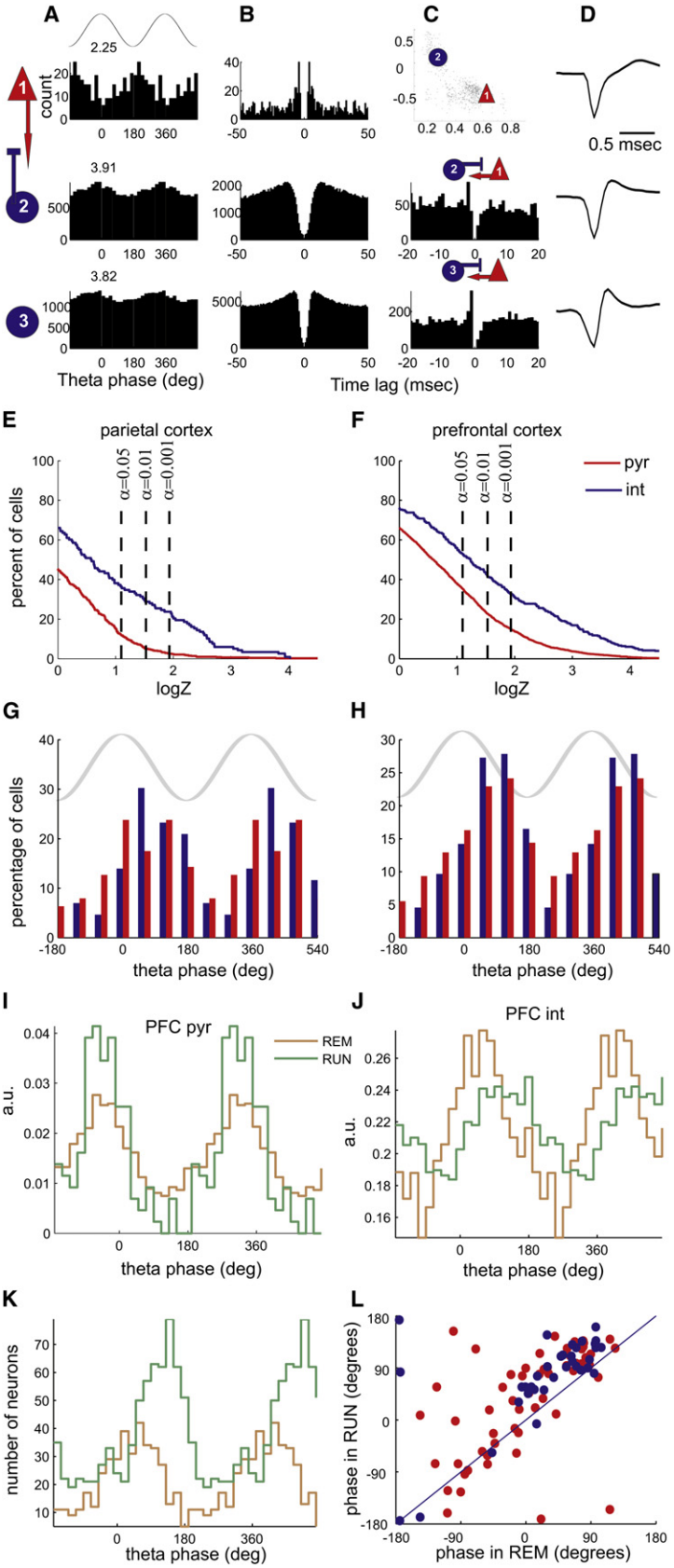

Figure 2. Hippocampal Theta Phase Modulation of Neocortical Neurons

(A–D) Each row corresponds to a single unit from the parietal-S1 area. (A) Theta phase histograms of neurons firing during REM sleep. Top, cartoon theta wave from the CA1 pyramidal layer. Numbers above, logZ statistics. Columns (B)–(D) characterize the units. (B) Autocorrelograms of the respective units. (C) Wave shape parameter scatterplot (top) and crosscorrelograms between the respective neuron and its monosynaptic partner (rows 2 and 3). (D) Average wideband-recorded (1 Hz–5 kHz) spike wave forms.

(E and F) Cumulative density function of phase modulation statistics (logZ) for putative pyramidal cells (pyr, red) and interneurons (int, blue) from the parietal (E) and mPFC (F). The plot is normalized to show the percentage of neurons (y axis) with logZ statistics greater than given value (*x* axis), y = P(X > x).

(G and H) Distribution of preferred phases for all significantly modulated ($p < 0.05$) neurons in the parietal cortex (G) and mPFC (H). Both cell types fire preferentially at around the peak/descending slope of hippocampal theta (phase 0°–90°).

(I and J), Theta phase histograms of an example pyramidal cell (I) and interneuron (J) from PFC during REM sleep and running on an elevated maze. Note that both neurons are significantly modulated in both states. Note also shift of phase preference of the interneuron.

(K) Phase histograms of preferred phases of all significantly modulated neurons during REM and awake running. Note phase shift of the population to the later theta phase during running.

(L) Scatterplot of preferred phases of neurons significantly modulated in both REM and RUN conditions (n = 98). Red, putative pyramidal cells; blue, putative inhibitory neurons.

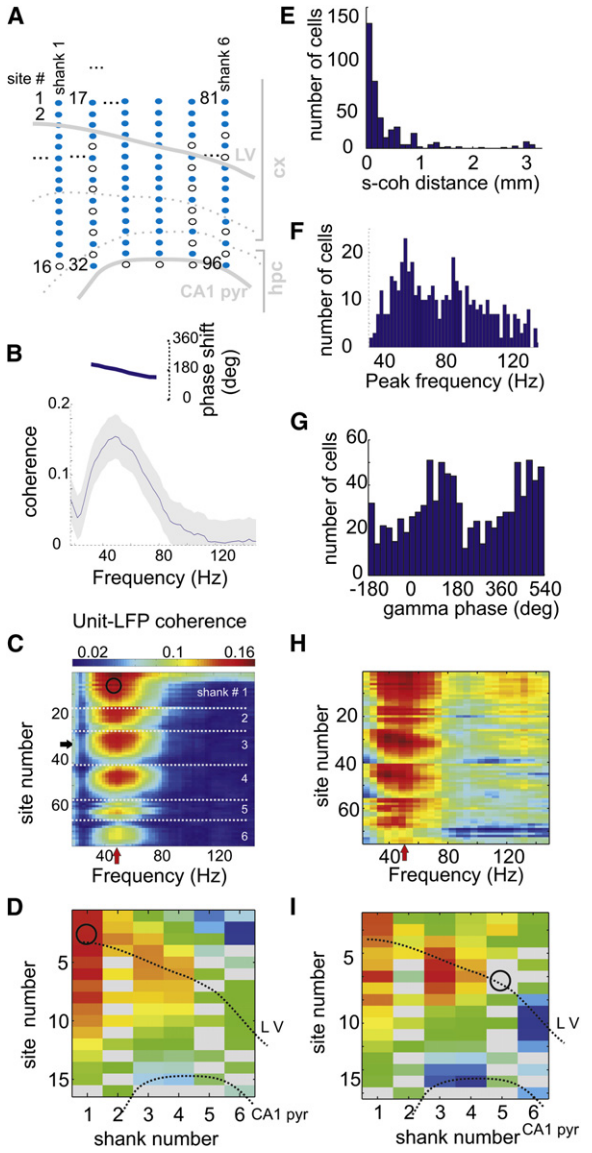

Figure 3. Gamma Frequency Band Synchronization of Neocortical Neurons

(A) Anatomical layout indicating the location of recording sites of the silicon probe used in the examples (B)–(D) and (H) and (I). Shanks are spaced by 300 μm, and each contains 16 recording sites 100 μm apart. Malfunctioning recording sites are shown as open circles and omitted from further analysis.

(B) Coherence (gray shading, 95 percentile confidence bands; inset, phase spectrum) between the spike train of a putative interneuron and the LFP at one recording site (horizontal arrow in [C]) in the parietal area.

(C) Coherence (color-coded) in the gamma range between a putative interneuron (recorded at site marked by a circle) and LFPs at all recording sites of the six shank silicon probe (y axis; 76 of 96; the remaining 20 sites with artifacts were excluded; see Supplemental Data). White dotted lines separate recording sites from adjacent shanks. Note increase of unit-LFP coherence at a preferred frequency (red vertical arrow, 40–50 Hz) and preferred depth/sites.

(D) Unfolding the unit-LFP coherence from (C) at the maximal frequency (red arrow in [C]) to a spatial map. The CA1 pyramidal layer and the approximate cortical layer 5 (dotted lines) are superimposed for spatial orientation. Circle, location of the soma of the recorded unit. Note that coherence (color) is highest locally and remains relatively high in a spatially contiguous volume up to 1 mm. Gray rectangles, sites with artifacts.

(E–G) Group statistics for all unit-LFP pairs with significant coherence (n = 456 units). (E) Distribution of the distances between the site of the recorded neuron (putative location of the soma) and the maximum unit-LFP coherence (s-coh distance). (F) Distribution of peak frequencies of unit-LFP coherence. (G) Distribution of preferred firing phases within the gamma cycle (trough, 180°).

(H and I) Example of spike triggered spectral analysis for a unit (same session as [A]–[D]). (H) Spike-triggered average power spectra (minus the power spectra calculated over the entire session; see Supplemental Data) color coded (red, relative increase of power; blue, relative decrease) for all channels (y axis). (I) Unfolding the spike-triggered power at preferred frequency from (H) to a spatial map. Circle, site of the recorded unit (putative soma location) used for triggering. Note that the power reaches maximum at a narrow "preferred" frequency band and at neighboring recording sites.

bursts is based on the covariance of spectral power in space (between different recording sites) and frequency (between different frequency bins, see Supplemental Data). Briefly, we performed factor analysis (principal component analysis followed by the Varimax rotation of the eigenvectors) of the spectral power in the gamma frequency range (30–150 Hz) seeking basis vectors that most parsimoniously captured the structure of power covariation between different frequency bins at different recording sites (Figures 3H, 3I, and 4D). The end product of this analysis was a set of factors, each of which was characterized by a vector of factor loadings reflecting the contribution of the respective frequency bins and recording sites to spectral power covariations. Projection of the spectra on these factors yielded a time series, termed factor scores, which reflect the strength of a given factor at any moment in time (Figure S7). Each of these factors could correspond to gamma oscillations with a distinct frequency and location pattern, and thus we refer to them as gamma frequency location (gFL) factors, or gFLs.

Several (from 0 to 32) gFLs were selected in each session based on explained covariance (Figure 5A). The space-frequency profiles of gFL factor loadings shared many features with those produced by unit-LFP spectral analysis and local maxima analysis. First, the gFL profiles showed a clear peak at a particular frequency and location (Figures 5B–5G). Second, some gFLs from the same recording session had similar frequencies but localized at different locations (Figures 5C, 5E, and 5G), while others displayed gamma oscillations of different frequencies at overlapping locations (Figures 5C, 5D, and 5G). Third, the spatial profiles of gFLs had elevated loading over several hundred micrometers, occasionally showing apparent localization in one cortical layer or a single cortical "column" (e.g., Figures 5C and 5E). Several location-frequency profiles of gFLs closely corresponded to those revealed by the unit-LFP spectral analysis (compare Figures 3C and 3D and Figures 5B and 5C) and local maxima analysis (Figure 4), confirming the validity of the method.

Hippocampal Theta Phase-Locking of Neocortical Gamma Oscillations

We next tested whether neocortical gamma oscillators are modulated by hippocampal theta. First, we found that the strongest theta modulation of neocortical gamma power occurred in a gamma frequency band higher than in the hippocampus (Figure 6A), eliminating volume-conduction of hippocampal gamma

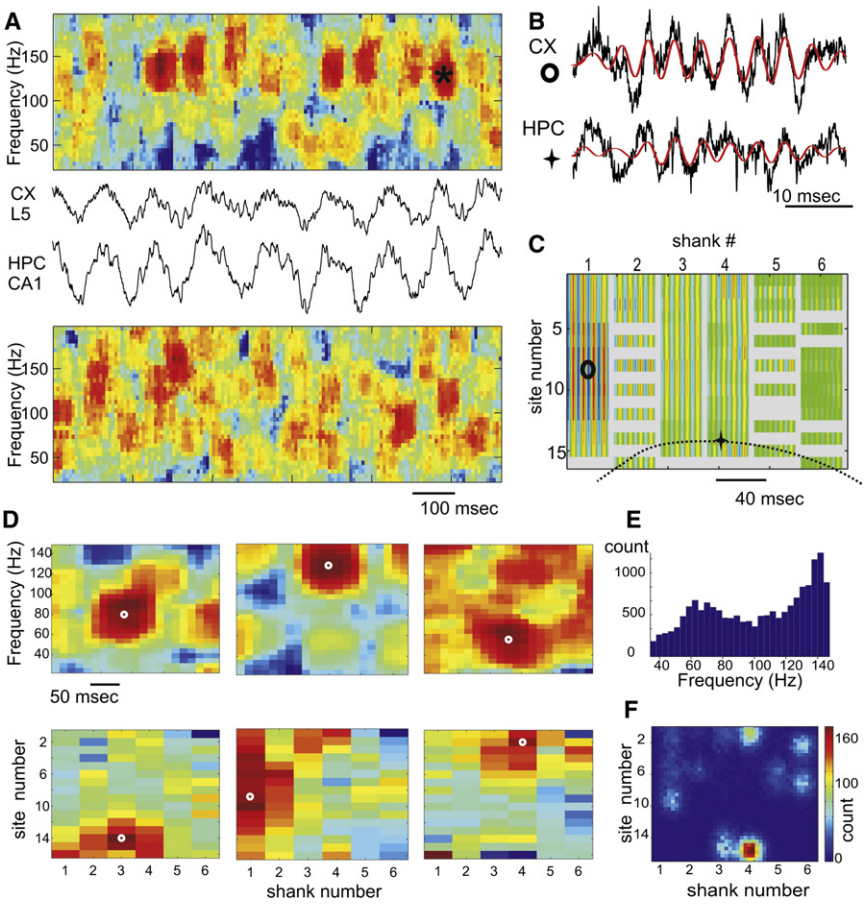

Figure 4. Temporal and Spatial Structure of Neocortical Gamma Oscillations

(A) A short epoch of neocortical (CX L5) and hippocampal (HPC CA1) LFPs and their associated "whitened" spectrograms.

(B) Gamma "burst" (red, band-pass,100–200 Hz, signal) from sites shown in (C).

(C) Color-coded spatial profile of band-pass-filtered segment in (B) at all recording sites (anatomical layout as in Figure 3A). Each column, separated by gray vertical stripes, corresponds to an electrode shank with 16 recording sites each. Malfunctioning sites are gray.

(D) Examples of isolated gamma bursts in hippocampus (left) and neocortex (middle, right). Each burst is characterized by a local maximum (white circles) of LFP spectral power (color) in both time-frequency (top) and anatomical space (bottom).

(E) Distribution of frequencies of individual local maxima. Note two modes, slow and fast gamma.

(F) Probability density of the spatial locations of local maxima of gamma power for the entire session. Note spatially segregated clusters.

to the neocortex as a potential confound. Second, in a subset of fast firing (>15 Hz) putative interneurons, we estimated the strength of unit-LFP gamma coherence at various time leads and lags from the peak of hippocampal theta (Figure 6B) and found maximum coherence on the descending slope of theta. Third, in a subset of experiments, we spatially isolated gamma bursts on the basis of power decay and clustered them in space and frequency (Figures 4D–4F). The probability of gamma bursts in some of these clusters was significantly biased by theta phase (Figure 6C). Although these separate approaches provided firm evidence for the theta phase modulation of neocortical gamma power, each of them had limitations. To overcome these limitations, we analyzed the relationship between the gFL factor score time series (which reflects the instantaneous strength of individual gamma oscillators; Figure S7) and hippocampal theta LFP (Figure 6D) and found significant coherence at theta frequency in a large fraction of the gFLs (e.g., Figure 6E). We also detected discrete times of gamma "burst" occurrence using the local maxima of the continuous gFL score time series. In a large percentage (~30%) of detected neocortical gFLs we found that gamma bursts were significantly phase modulated by hippocampal theta with the highest incidence near the peak of theta (Figures 6F–6H). High-frequency neocortical gamma bursts (>100 Hz) had stronger theta modulation and theta phase preference at a later phase (~50°; Figure 6I) than lower-frequency gamma oscillations. As expected from unit analysis, hippocampal gFL-bursts were more likely to be significantly modulated by hippocampal theta than those localized in the neocortex (60% versus 30%; Figure 6G).

Because the gFL analysis does not exploit the phase in the LFP signal, it can still be biased by the volume conduction of hippocampal gamma to the neocortex. We performed a number of analyses to rule out the contribution of the volume-conduction (see Supplemental Data). First, we estimated coherence between the gFL score and hippocampal LFP by partializing it by the hippocampal gamma power corresponding to the frequency range of the respective gFL. Approximately 90% of all gFLs (>98% for high frequency gFLs) retained a significant peak in the theta band. Second, for each gFL we computed coherence between the LFP in the center of the gFL-identified spatial gamma profile and at all other sites. The peak coherence occurred at the frequency close to the preferred frequency of the gFL (Figures S8A and S8B), with a spatial profile that matched that of the gFL (Figure 6J), providing a direct phase-synchronization measure of the local neocortical gamma. Next, we computed the integrated gamma LFP-LFP coherence within the gFL preferred frequency band in short sliding windows for the entire session and estimated the coherence between this time series and hippocampal LFP for each pair of recording sites (Figure 6K). The significant peaks at theta frequency revealed theta modulation of gamma synchronization between the LFP in the center of the gFL and spatially contiguous recording sites. If modulation of gamma power in the neocortex was a result of volume conduction of currents from the hippocampus one would expect that theta modulation of LFP-LFP coherence would increase toward hippocampus. However, in most cases the spatial profile of theta modulation of LFP-LFP gamma coherence closely matched that of the gFL and average LFP-LFP gamma

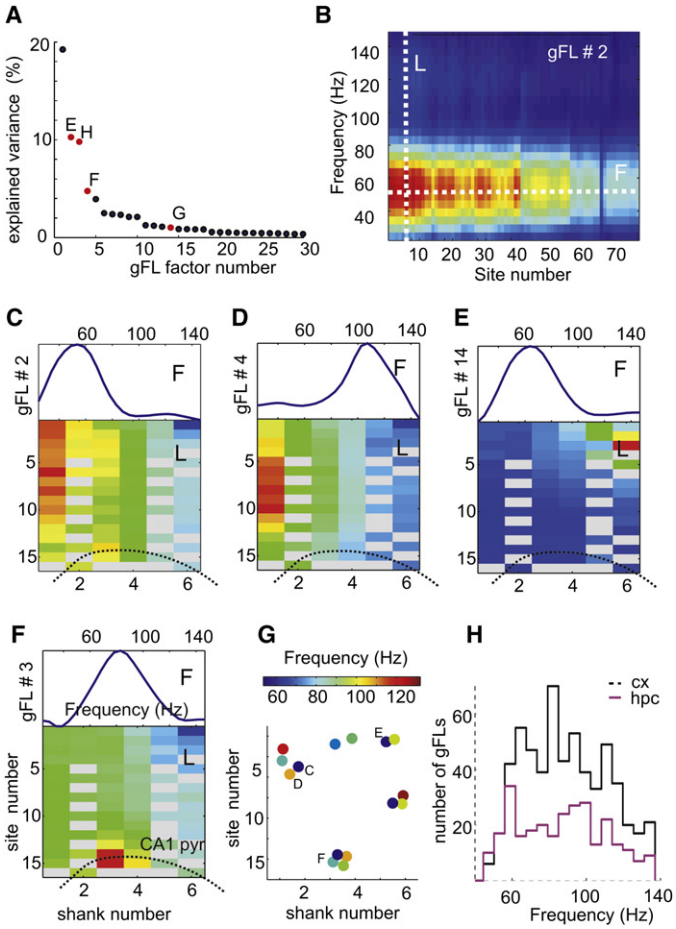

Figure 5. Spatial and Frequency Heterogeneity of Neocortical Gamma Oscillations

(A–G) Frequency-location gamma power (gFL) factor analysis (see Supplemental Data). (A) Percentage of total variance explained by the first 30 gFL factors. (B) Color-coded gFL factor loadings at 76 recording sites of the six shanks (20 malfunctioning sites removed) and gamma frequency bins (30–150 Hz). Red, positive, and blue, negative loading values. Maximal loading is localized at a given frequency (white line F) and location (white line L). (C–F) Examples of gFL factor loadings represented by frequency profile (F, top plots, loading at the maximal site across frequencies) and location profile (L, bottom, spatial maps; color indicates loading at the maximal frequency across sites) in the neocortex (C–E) and hippocampus (F). (G) Frequency (color) and spatial location of the center of mass of gFL components in a single session. Note spatial clusters of different frequency gFLs (e.g., C, D) or similar frequency preference but different locations (e.g., C, E).

(H) Distribution of the preferred frequency of cortical (n = 588, black) and hippocampal (n = 285, magenta) gFL factors.

coherence (e.g., compare Figure 5D and Figures 6J and 6K). The phase shift between gamma synchronization signal and hippocampal LFP was larger for the fast gamma, consistent with the phase preference analysis of gFL bursts (Figures S8C and S8D). Third, the spatial location of gFLs, the magnitude of theta modulation and the preferred theta phase of gFL-identified gamma bursts were similar between the first and second halves of the recording session (Figure S9), indicating that each gFL score represents the time course of an independent process. Finally, we identified a number of theta modulated gFLs in PFC, where volume-conduction of gamma is not expected due to its distance from the hippocampus. Overall, these findings indicate that hippocampal theta oscillations can exert a significant effect on local computation, represented by location and frequency-specific gamma oscillations, in wide neocortical areas.

Theta Modulation of the Membrane Potential in Neocortical Neurons

Theta phase modulation of neocortical unit discharges and gamma activity should be reflected by the membrane potential fluctuations in single neurons. To test this hypothesis, we obtained stable intracellular recordings from deep layer S1 neurons (n = 4) and biocytin-filled pyramidal cells in the mPFC (layer 2 = 1; layer 5 = 15; layer 6 = 7), together with simultaneous LFP recordings from the hippocampal CA1 pyramidal layer in an additional 27 rats anesthetized by urethane/ketamine-xylazine (Isomura et al., 2006). Hippocampal theta (3–5 Hz under anesthesia) occurred either spontaneously or was induced by tail pinching. Theta frequency oscillations of the membrane potential occurred transiently in several neocortical neurons. The intracellular voltage fluctuations occurred coherently with hippocampal theta in 16 out of 27 neurons (Figures 7A–7E). Spectral analysis of the membrane potential oscillations revealed significant power in the gamma frequency band, which fluctuated coherently with hippocampal theta (10 out of 27; Figures 7B and 7D). Both phase and strength of theta phase modulation of the membrane potential and the intracellular power of gamma were correlated with each other, although the coherence between the LFP and the membrane potential was stronger than that between the LFP and the gamma power (p = 0.004; Figures 7F and 7G). These analyses of intracellular data confirm that hippocampal theta oscillation can modulate the activity of neocortical neurons.

Volume Conduction of Hippocampal Theta Currents to the Neocortex

LFP theta oscillations in the parietal area were consistently present whenever hippocampal theta was observed, and the two theta signals co-varied in both frequency and magnitude. To examine whether LFP theta was generated by the neocortical circuits independent of hippocampal theta, we analyzed simultaneous LFP recordings in the hippocampus-neocortex axis, using multiple-site silicon probes (n = 21 sessions; Figures 8A1 and 8A2) and epidural grids (n = 9 sessions; Figures 8B1 and 8B2). In support of previous observations in anesthetized animals (Bland and Whishaw, 1976; Gerbrandt et al., 1978), the average magnitude of theta power monotonically decreased with distance from the hippocampus (Figure 8A3), and the distribution of theta power on the cortical surface reflected the physical layout of the underlying hippocampus (Figure 8B3). Theta power decreased, on average, 30%/mm in vertical direction and only 5%–10%/mm along the surface of the brain (Figure 8C). Both epidural and depth LFPs were strongly coherent with hippocampal LFP at theta frequency, with coherence

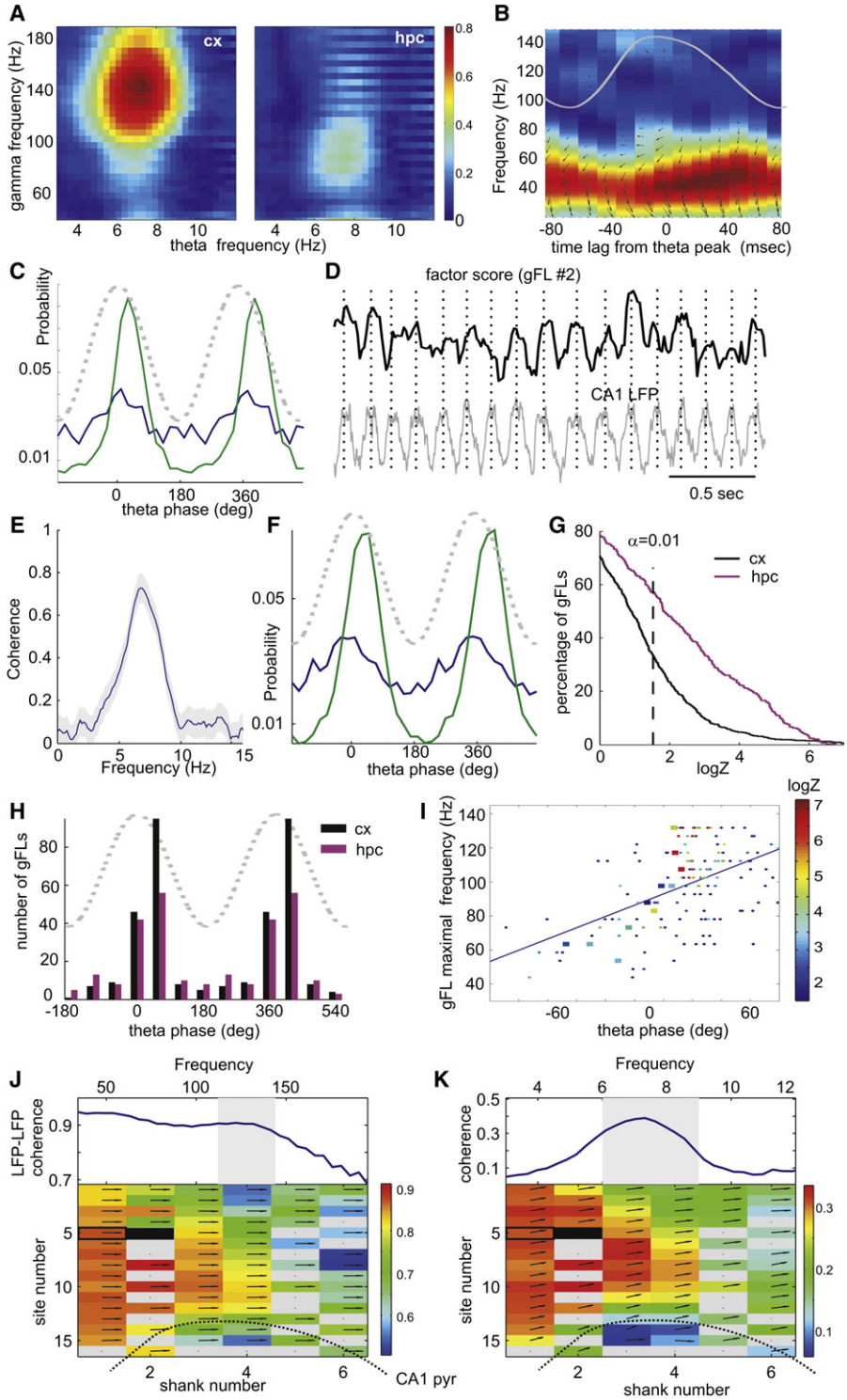

Figure 6. Hippocampal Theta Oscillations Modulate Neocortical Gamma

(A) Color-coded coherence between theta LFP in hippocampus and gamma power in different frequency bins (y axis) in the neocortex (cx) and hippocampus (hpc). Note strong modulation of higher-frequency gamma in the neocortex.

(B) Spike-LFP gamma band coherence (same unit-site pair as in Figure 3B) as a function of time lag from the peak of hippocampal theta (superimposed gray line). Small arrows, phase of spikes related to local gamma waves (zero is 3 o'clock).

(C) Theta phase histograms for two clusters of isolated gamma busts (Figures 4 E and 4F), whose spatial and frequency features correspond to those of gFL factors in Figures 5C and 5D. Dashed line, theta phase.

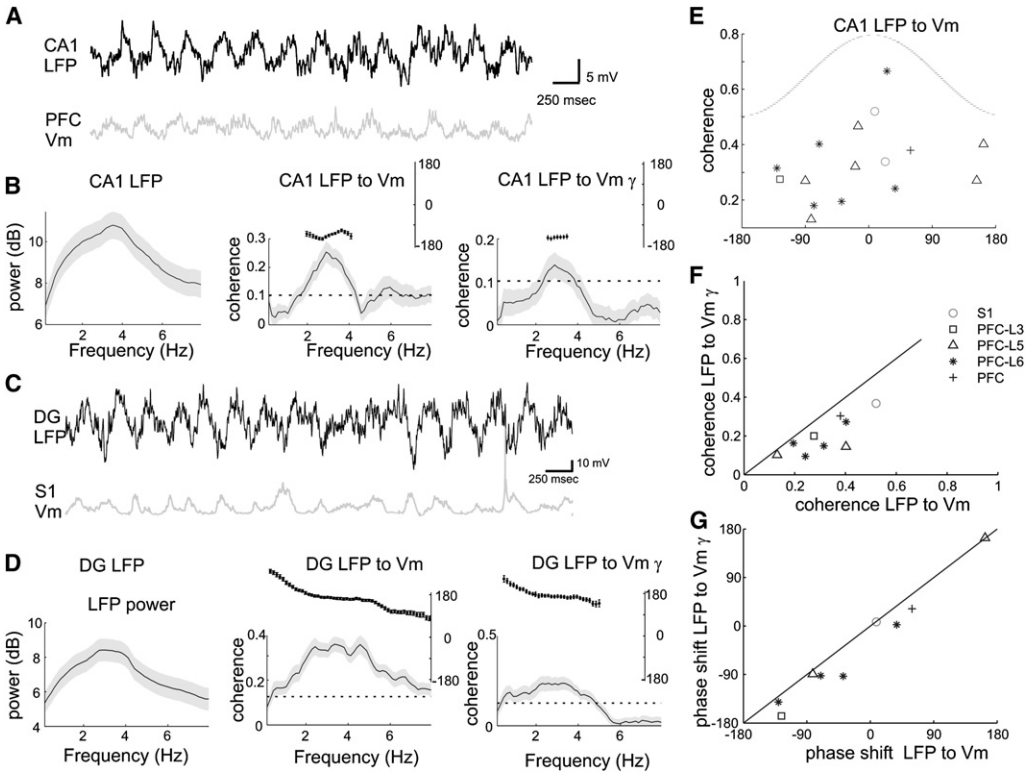

Figure 7. Theta phase Modulation of Membrane Potential in Neocortical Neurons under Anesthesia

(A) Simultaneous recording of LFP in the CA1 pyramidal layer and intracellularly recorded membrane potential in a layer 5 PFC neuron (PFC Vm).

(B) Power spectrum of the LFP (gray shading, 95 percentile confidence intervals, left); coherence between the LFP and the PFC Vm (middle); coherence between the LFP and integrated gamma power in PFC Vm (right); Inset, phase shift for the significantly coherent frequency band.

(C and D) Same display as in (A) and (B) for the simultaneous recording of LFP in the dentate gyrus (DG; theta phase ~160 degrees shifted from that in CA1) and intracellular recording from a layer 5 neuron in S1.

(E) Scatter plot of the phase shift versus the coherence value at the peak coherence frequency between CA1 LFP and Vm in cortical neurons (n = 16 significantly coherent neurons). Zero phase shift corresponds to depolarization in the Vm at the peak of hippocampal CA1 theta.

(F) Relationship between two coherence measures; coherence between the LFP and Vm versus coherence between the LFP and integrated Vm gamma power (both passed significance test).

(G) Relationship between phase shifts for cells in (F). S1, somatosensory area; PFC-L3, -L5, -L6, layers 3 to 6 of mPFC.

decaying at a rate of 5%–10%/mm (Figure 8D). Theta waves recorded between the CA1 pyramidal layer and cortical surface had approximately the same phase at all recording sites (Figure 8A4). However, the phase difference increased as a function of distance from the hippocampus in lateral and posterior directions up to 60° (e.g., Figure 8B4; n = 4 rats). Commensurate with these observations, current-source density analysis of LFP did not yield significant local sinks or sources in the theta band in the parietal area overlying the hippocampus. These findings suggest that theta measurements in the rodent neocortex are

(D) Short epoch of hippocampal theta oscillation (LFP) and factor score time series for a representative neocortical gFL (shown in Figure 5C).

(E) Coherence spectrum between the hippocampal LFP and the neocortical gFL score time series shown in (D).

(F) Theta phase histograms of neocortical "gamma bursts" (the peaks of the factor score time series) for gFLs shown in Figures 5C and 5D. Note the similarity between (C) (local maxima-based) and (F) (gFL-based) gamma burst identification.

(G) Cumulative density functions of theta phase modulation strength (logZ) for gamma bursts localized in the neocortex (black) and the hippocampus (magenta).

(H) Distribution of preferred phases of significantly ($p < 0.01$) theta-modulated gamma bursts in the neocortex (n = 280 out of 588 gFLs; black) and the hippocampus (n = 188 out of 285 gFLs; magenta).

(I) Scatterplot of the preferred theta phase of significantly modulated neocortical gamma bursts against their preferred frequency. Color indicates the strength of theta modulation statistic logZ (dots, all data; large squares, single session). Note that high-frequency gamma bursts occur at the later theta phase.

(J) Bottom, spatial map of average coherence between the LFP at the site (solid rectangle) in the center of a gFL in Figure 5D) and other sites at the gFL preferred frequency (shaded area). Top trace, example coherence for one site (open rectangle). Arrows, phase shift (zero at 3 o'clock).

(K) Top, coherence between theta LFP and gamma coherence between two neocortical sites (open rectangle and center of gFL, solid rectangle). Integrated gamma LFP-LFP coherence within the frequency band of maximum coherence (shaded range in [J]) was first computed in short sliding windows and the coherence between the resulting time series and hippocampal LFP is displayed here. Integral of this coherence in the shaded area quantifies theta modulation of gamma LFP-LFP coherence. Bottom, spatial map of theta modulation of coherence between the gFL center site (black) and other sites. See also Figure S10.

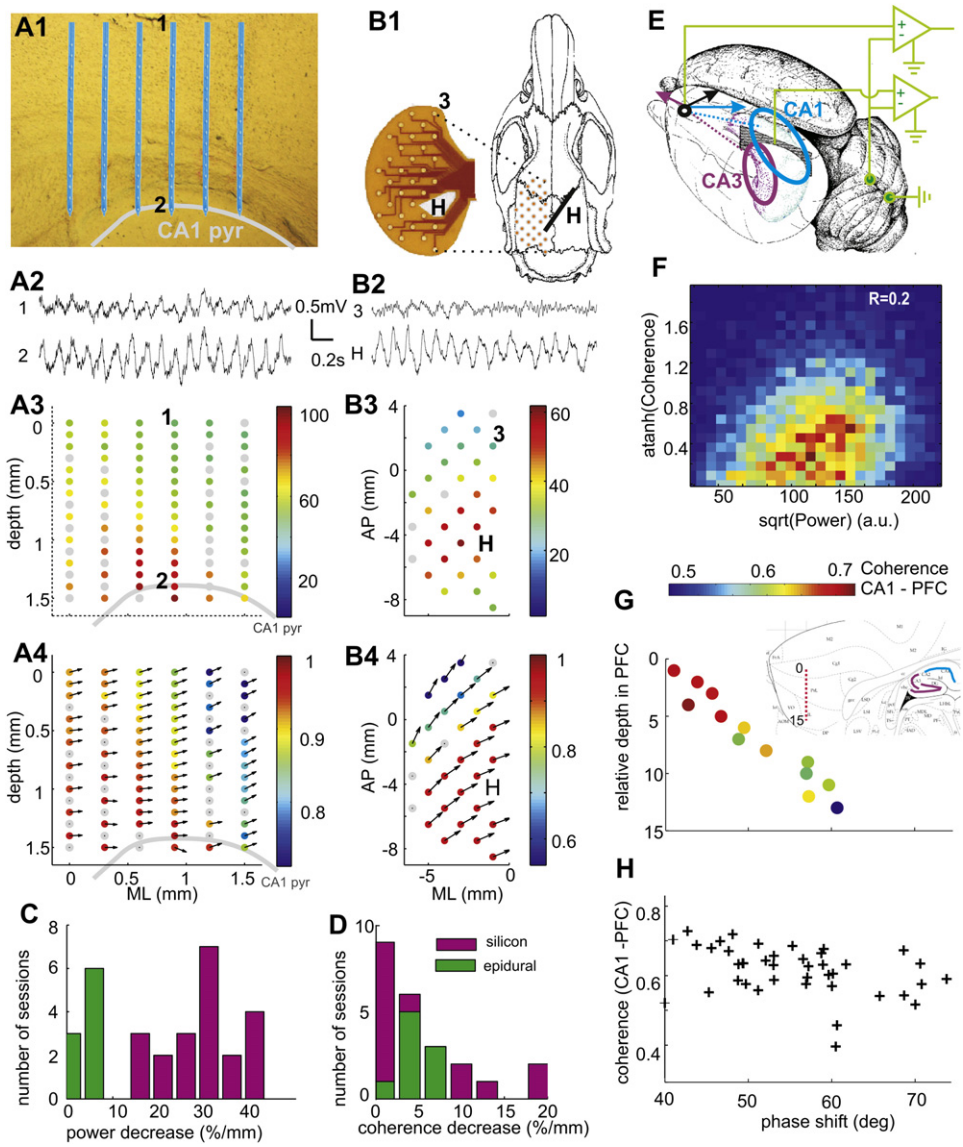

Figure 8. Volume-Conducted Hippocampal Theta Signals in the Neocortex

(A1) Position of probe shanks in the neocortex and CA1 pyramidal layer (highlighted by gray line). (A2) LFP signals from the supragranular layer of neocortex (1) and hippocampus (2). Two-dimensional map of theta power (normalized, A3) and coherence between site 2 (CA1 pyr) and other sites (A4). Theta phase shifts are indicated by arrows. Zero phase difference corresponds to 3 o'clock direction.

(B1) Layout of epidural recording of surface LFP with a flex cable (photo left). H, hippocampal depth electrode. (B2) LFP signals from site 3 of neocortex (3) and hippocampus (H). Two-dimensional map of surface theta power (B3) and coherence (B4).

(C and D) Distribution of the rate of power decrease (C) and rate coherence decrease (D) across experiments with silicon probe recordings (vertical axis, magenta) and epidural grids (horizontal axis, green).

(E) Lateral-posterior view of the left hemisphere. Arrows, hypothetical contribution of volume-conducted theta LFP vectors in PFC from the CA1 and CA3 regions (ellipsoids). The locations of ground and reference screw electrodes are also shown.

(F) Joint probability density of LFP theta power in CA1 pyr. layer and coherence between CA1 and mPFC LFP in one awake running session. Rank correlation coefficient $R = 0.2$, $p < 0.0001$.

(G) Relationship between CA1-PFC theta phase shift (coherence color-coded) and recording depth in PFC. Inset, location of the recording sites (red dots) in a sagittal section of PFC. Note monotonic phase shift and decreasing coherence with relative depth.

(H) Scatterplot of coherence between CA1 and PFC signals versus theta phase shift (n = 5 rats; REM and wake sessions combined).

dominated by the currents that are volume-conducted from the hippocampus (Bland and Whishaw, 1976; Gerbrandt et al., 1978).

LFP in the more anterior mPFC region was typically "flat" during continuous hippocampal theta oscillations (Jones and Wilson, 2005; Siapas et al., 2005) and only occasionally displayed

visible transient periods (0.5–2 s) of theta frequency oscillations (e.g., Figure 8B2). Although these intermittent theta periods were associated with increased coherence between hippocampus and PFC LFP, their occurrence was positively correlated with the power increases of hippocampal theta (Figure 8F; n = 44 sessions, rank correlation R = 0.2 ± 0.07). Moreover, LFP recorded at various depths in mPFC showed a linear phase shift and decreasing coherence referenced to the CA1 pyramidal layer (Figure 8G). Across experiments, the average CA1-mPFC coherence in the theta range was ~0.7 and the phase shift ranged from 40° to 70° (n = 25 sessions; Figure 8H). Importantly, coherence between PFC unit activity and hippocampal LFP, on average, was generally higher than the coherence between unit firing and locally recorded LFP.

Several aspects of the observations in mPFC are consistent with a volume-conductor model containing two (or more) distributed sources: e.g., CA1 and CA3/dentate regions of the hippocampus, and entorhinal cortex. Since LFP in the CA3 pyramidal layer is phase shifted (~150°) relative to CA1 pyramidal layer (cf. Buzsáki, 2002), the amplitude, phase, and coherence of theta at any location in the brain is determined by the vector summation of two (or more) volume-conducted currents (Figure 8E) and thus by the relative strength and phase of the theta generators and their relative distances from the recording site.

DISCUSSION

The major finding of the present experiments is that hippocampal theta oscillations can effectively bias the timing of local computation in the neocortex. A fraction of neurons in different neocortical areas, including the primary somatosensory area and PFC, as well as spatially localized and frequency-specific gamma oscillations were phase locked to hippocampal theta oscillations. These data suggest that theta oscillation entrainment provides a mechanism by which activity in spatially widespread neocortical and hippocampal networks can be temporally coordinated.

Hippocampal Theta Phase Locking of Neocortical Neurons

A robust finding of our experiments in both rats and mice is that 5% to 40% of neocortical neurons were significantly phase locked to hippocampal theta oscillations during either exploration or REM sleep. Importantly, theta-modulated neurons were found not only in the PFC which has massive direct afferents from the hippocampus (Swanson, 1981), but also in the primary somatosensory area, which has only multisynaptic connections with the hippocampus (Witter, 1993; Cenquizca and Swanson, 2007). The overall fraction of theta-locked units in the PFC (~35%) is comparable to that reported previously (Siapas et al., 2005), although the identity of units was not characterized in that study. These numbers should be contrasted to those in the hippocampus where, in the CA1 region, approximately 80% of the pyramidal cells and more than 90% of interneurons are significantly phase locked to theta oscillations (Figure S10; Csicsvari et al., 1999). In addition, the strength of theta modulation was considerably weaker in the neocortex, especially in the parietal cortex. These observations support the hypothesis that firing of neurons in many cortical areas is biased by the hippocampal theta oscillations (Miller, 1991).

Theta phase-locking of neocortical neurons can be brought about by multiple potential mechanisms. The simplest and oldest model assumes an independent pacemaker, residing in the septal complex (Petsche et al., 1962) and/or the supramammillary nucleus (Kocsis and Vertes, 1994), and recent studies suggest that a portion of neocortex-projecting neurons in the basal forebrain are phase-locked to hippocampal theta (Lee et al., 2005; Lin et al., 2006). An alternative mechanism of theta entrainment of distant neocortical neurons may entail the utilization of the entorhinal cortex and/or the PFC by way of their widespread, mostly reciprocal, connections with numerous neocortical regions (Groenewegen and Uylings, 2000; Swanson, 1981; Swanson and Kohler, 1986; Thierry et al., 2000; Witter, 1993). A final possibility is that hippocampo-neocortical coordination is brought about by the class of sparse long-range hippocampal projections to distant neocortical regions (Cenquizca and Swanson, 2007; Jinno et al., 2007). Any of these pathways alone or in combination may impose the hippocampal rhythmic output on their targets. The selective entrainment of a subset of neocortical neurons may be explained by either stronger synaptic connectivity between the hippocampus and selected target neocortical neurons or by the intrinsic properties of neuronal subgroups (Beierlein et al., 2000; Blatow et al., 2003; Gutfreund et al., 1995; Ulrich, 2002). Furthermore, various pharmacological manipulations can evoke theta-frequency oscillations in neocortical slices (Bao and Wu, 2003; Flint and Connors, 1996; Silva et al., 1991). Thus, theta oscillations in neocortical structures may emerge locally or/and phase-synchronize with the hippocampus via the above conduits.

The stronger entrainment of interneurons by hippocampal theta may also contribute to the enhancement of gamma oscillations (Beierlein et al., 2000; Csicsvari et al., 2003; Gibson et al., 1999; Hasenstaub et al., 2005). The similar theta phase preference of pyramidal cells and interneurons can be explained by either assuming that rhythmic afferents activated the two populations in a feed-forward manner or that local circuits are also involved in the generation of theta activity, similar to that in the CA3 hippocampal region (Buzsáki, 2002; Konopacki et al., 1987).

Locally Generated Neocortical Gamma Oscillations

Previous work has established that engagement of local circuits is reflected by the transient emergence of local gamma frequency oscillations (Bragin et al., 1995; Engel et al., 2001; Gray and Singer, 1989). We used several methods to explore neocortical gamma oscillations and demonstrated their local origin. In contrast to the hippocampus (Bragin et al., 1995; Csicsvari et al., 2003), gamma oscillations in the neocortex were transient and highly localized, confirming similar observations made with subdural grid recordings in humans (Canolty et al., 2006; Edwards et al., 2005; Howard et al., 2003; Menon et al., 1996; Sederberg et al., 2003). The amplitude of gamma oscillations decreased rapidly with distance. Gamma oscillators were often localized to either a single cortical layer and/or a putative column, consistent with previous reports (Gray and Singer, 1989; Steriade and Amzica, 1996; Sukov and Barth, 1998). Emergence of these transient fast rhythms faithfully reflects behaviorally relevant specific

computation in small networks (e.g., Gray and Singer, 1989; Montgomery and Buzsáki, 2007; Pesaran et al., 2002; Schoffelen et al., 2005; Sederberg et al., 2003). Our findings demonstrate that hippocampal theta oscillations can effectively link these sporadic and spatially distinct local gamma oscillations.

Hippocampal Theta Phase Locking of Neocortical Gamma Oscillations

Previous work has shown crossfrequency coupling between theta and gamma rhythms in the hippocampus (Bragin et al., 1995) and entorhinal cortex (Chrobak and Buzsáki, 1998a; Mormann et al., 2005). Recently, theta-gamma coupling was reported in the temporoparietal lobe of epileptic patients as well (Canolty et al., 2006). Intracranial recordings in patients also showed coupling between single unit activity and oscillations of various frequencies in the theta-gamma range (Jacobs et al., 2007). Furthermore, ''midline theta oscillations'' in human scalp recordings (Gevins et al., 1979) as well as isolated, transient neocortical theta oscillations in subdural and intracranial recordings during performance in various cognitive tasks have also been described (Caplan et al., 2003; Kahana et al., 1999; Raghavachari et al., 2001; Rizzuto et al., 2003), However, neither the mechanisms nor the origin of theta signals could be demonstrated in these clinical studies. Simultaneous recordings from the hippocampus and neocortex in our studies established that hippocampal theta oscillations exert an effect on local neocortical computation by rhythmically biasing synchrony of local gamma oscillations. We also found that neocortical fast gamma oscillations (80–150 Hz) were more strongly modulated by theta and occurred at a later phase (~50 degrees). This observation suggests that at least two distinguishable mechanisms can generate gamma oscillations in the neocortex with the higher frequency mechanism more responsive to hippocampal output (Wyart and Tallon-Baudry, 2008). The effect of theta phase-locked output on neocortical network dynamics may be analogous to that of a sensory stimulus (Engel et al., 2001; Gray and Singer, 1989; Sukov and Barth, 1998) since both effects can induce localized gamma oscillations. The widespread synchronization of neocortical neuronal assemblies by the hippocampal theta rhythm might provide a mechanism for ''gating'' of sensory information and temporally biasing movement initiation by the hippocampal theta rhythm (Bland, 1986).

Volume Conduction of Hippocampal Theta to the Neocortex

Using a combination of approaches, including epidural grid and silicon probe recordings of LFP, our findings support previous suggestions that theta signals in a large expanse of the rat neocortex and other proximal structures are largely volume conducted from the hippocampus and/or entorhinal cortex (Bland and Whishaw, 1976; Gerbrandt et al., 1978). Coherence of theta signals was attenuated monotonically as a function of both vertical and horizontal distance from the hippocampus, with a predictable phase shift between hippocampal and neocortical recording sites. If theta signal represented a single periodic dipole and originated from a point source, its attenuation and phase could be calculated from the biophysical features of the conducting brain tissue (Logothetis et al., 2007). However, theta is a consortium of several oscillators generated by multiple hippocampal-entorhinal regions and mechanisms, and both the power and phase relation of the generators vary as a function of behavior (Buzsáki, 2002). The important consequence of this complex relationship is that LFP signals recorded from cortical or subcortical sites in the rodent may reflect superposition of volume-conducted currents from two or more spatially distributed current sources in the hippocampus (Figure 8E) and the entorhinal cortex. The implication of the multiple-source volume-conductor model is that the amplitude, phase, and degree of coherence to hippocampal theta of extrahippocampally recorded theta signals may show systematic variations with behavior, yet such changes may arise entirely from intrahippocampal mechanisms.

These observations and considerations, of course, do not exclude neocortical generation of theta oscillations (Caplan et al., 2003; Ishii et al., 1999; Kahana et al., 1999; Raghavachari et al., 2001; Rizzuto et al., 2003). Importantly, we found that a small portion of PFC theta bursts was different in frequency from hippocampal theta (not shown), indicating that PFC circuits can generate LFP in the theta frequency band (Siapas et al., 2005; Jones and Wilson, 2005). However, when such transient epochs are of the *same* frequency as hippocampal theta, disambiguating locally generated currents and volume-conducted currents becomes difficult with currently available LFP recording methods.

Reciprocal Information Transfer by Theta Oscillations

Transfer of information in the brain from source (sender) to target (receiver) is usually considered unidirectional: the source network sends the information to a recipient network (Abeles, 1991). Oscillatory entrainment, however, allows for a different mechanism of information exchange, which we refer to as ''reciprocal information transfer.'' In this hypothetical mechanism, we assume that the recipient structure plays an initiating role by temporally biasing activity in the source structure, creating time windows within which the recipient structure can most effectively receive information (Fries, 2005; Isomura et al., 2006; Sirota et al., 2003; Sirota and Buzsáki, 2007; Womelsdorf et al., 2007). For example, experiments suggest that during slow wave sleep transfer of hippocampal information to the neocortex is initiated by the down-up transition of neocortical slow oscillation (Isomura et al., 2006; Sirota et al., 2003; Sirota and Buzsáki, 2007). In a similar manner, we suggest that transfer of neocortical information to the hippocampus is actively initiated by the hippocampus via theta-phase biasing of neocortical network dynamics. As a result, self-organized gamma oscillations at multiple cortical locations is temporally biased so that the information contained in the gamma bursts would arrive at the hippocampus at the phase of the theta cycle when the network can be perturbed maximally and when it is most plastic (Holscher et al., 1997; Huerta and Lisman, 1996; Hyman et al., 2003), which, in the case of CA1 pyramidal cells, corresponds to the positive (least active) phase of the theta cycle (Csicsvari et al., 1999). In this context, it is noteworthy that hippocampal neurons begin to discharge at this late (positive) phase when the rat enters the place field of the neuron (O'Keefe and Recce, 1993), likely triggered by the cooperative action of neocortical assemblies.

The postulated model of reciprocal information transfer can ensure that information from wide areas of the neocortex can be presented to the hippocampus in a temporally synchronous manner and integrated into its associative networks.

EXPERIMENTAL PROCEDURES

Animals and Recording

Chronic recordings in the neocortex and hippocampus using silicon probes, tetrodes, or epidural electrodes were performed in rats (n = 28) and mice (n = 11) during sleep and waking behavior. Acute extracellular recordings in the hippocampus and intracellular recordings in the neocortex were performed in anesthetized rats (n = 27; Isomura et al., 2006).

Data Analysis

All analysis was performed using custom-written tools in Matlab (Mathworks). For detailed description, see Supplemental Data.

SUPPLEMENTAL DATA

The Supplemental Data include Ten Figures and Supplemental Experimental Procedures and can be found with this article online at http://www.neuron.org/supplemental/S0896-6273(08)00762-9.

ACKNOWLEDGMENTS

We thank Asohan Amarasigham, Carina Curto, Kamran Diba, Caroline Geisler, Kenji Mizuseki, Simal Ozen, Lucas Parra, and Alfonso Renart for useful discussions and comments on the manuscript; Derek Buhl and Dirk Isbrandt for providing recordings in mice; Alexei Ponomarenko and Matthew Guilfoyle for assisting with recordings; Darrell A. Henze for intracellular recordings from somatosensory cortex; and John Bentley and Michael Stephens for help with statistical analysis of the mixture model. Supported by National Institutes of Health (NS034994; MH54671), National Science Foundation (SBE0542013), the J.D. McDonnell Foundation, Uehara Memorial Foundation, and the Japan Society of Promotion for Sciences.

Accepted: September 4, 2008
Published: November 25, 2008

REFERENCES

Abeles, M. (1991). Corticonics: Neural Circuits of the Cerebral Cortex (Cambridge: Cambridge University Press).

Alonso, A., and Garcia-Austt, E. (1987). Neuronal sources of theta rhythm in the entorhinal cortex of the rat. II. Phase relations between unit discharges and theta field potentials. Exp. Brain Res. *67*, 502–509.

Anderson, M.I., and O'Mara, S.M. (2003). Analysis of recordings of single-unit firing and population activity in the dorsal subiculum of unrestrained freely moving rats. J. Neurophysiol. *90*, 655–665.

Bao, W., and Wu, J.Y. (2003). Propagating wave and irregular dynamics: spatiotemporal patterns of cholinergic theta oscillations in neocortex in vitro. J. Neurophysiol. *90*, 333–341.

Barthó, P., Hirase, H., Monconduit, L., Zugaro, M., Harris, K.D., and Buzsáki, G. (2004). Characterization of neocortical principal cells and interneurons by network interactions and extracellular features. J. Neurophysiol. *92*, 600–608.

Beierlein, M., Gibson, J.R., and Connors, B.W. (2000). A network of electrically coupled interneurons drives synchronized inhibition in neocortex. Nat. Neurosci. *3*, 904–910.

Berg, R.W., Whitmer, D., and Kleinfeld, D. (2006). Exploratory whisking by rat is not phase locked to the hippocampal theta rhythm. J. Neurosci. *26*, 6518–6522.

Bland, B.H. (1986). The physiology and pharmacology of hippocampal formation theta rhythms. Prog. Neurobiol. *26*, 1–54.

Bland, B.H., and Whishaw, I.Q. (1976). Generators and topography of hippocampal theta (RSA) in the anaesthetized and freely moving rat. Brain Res. *118*, 259–280.

Blatow, M., Rozov, A., Katona, I., Hormuzdi, S.G., Meyer, A.H., Whittington, M.A., Caputi, A., and Monyer, H. (2003). A novel network of multipolar bursting interneurons generates theta frequency oscillations in neocortex. Neuron *38*, 805–817.

Bragin, A., Jando, G., Nadasdy, Z., Hetke, J., Wise, K., and Buzsáki, G. (1995). Gamma (40–100 Hz) oscillation in the hippocampus of the behaving rat. J. Neurosci. *15*, 47–60.

Buño, W., Jr., and Velluti, J.C. (1977). Relationships of hippocampal theta cycles with bar pressing during self-stimulation. Physiol. Behav. *19*, 615–621.

Buzsáki, G. (2002). Theta oscillations in the hippocampus. Neuron *33*, 325–340.

Buzsáki, G. (2006). Rhythms of the Brain (New York: Oxford University Press).

Canolty, R.T., Edwards, E., Dalal, S.S., Soltani, M., Nagarajan, S.S., Kirsch, H.E., Berger, M.S., Barbaro, N.M., and Knight, R.T. (2006). High gamma power is phase-locked to theta oscillations in human neocortex. Science *313*, 1626–1628.

Caplan, J.B., Madsen, J.R., Schulze-Bonhage, A., Aschenbrenner-Scheibe, R., Newman, E.L., and Kahana, M.J. (2003). Human theta oscillations related to sensorimotor integration and spatial learning. J. Neurosci. *23*, 4726–4736.

Cenquizca, L.A., and Swanson, L.W. (2007). Spatial organization of direct hippocampal field CA1 axonal projections to the rest of the cerebral cortex. Brain Res. Brain Res. Rev. *56*, 1–26.

Chrobak, J.J., and Buzsáki, G. (1998a). Gamma oscillations in the entorhinal cortex of the freely behaving rat. J. Neurosci. *18*, 388–398.

Chrobak, J.J., and Buzsáki, G. (1998b). Operational dynamics in the hippocampal-entorhinal axis. Neurosci. Biobehav. Rev. *22*, 303–310.

Collins, D.R., Lang, E.J., and Paré, D. (1999). Spontaneous activity of the perirhinal cortex in behaving cats. Neuroscience *89*, 1025–1039.

Colom, L.V., Christie, B.R., and Bland, B.H. (1988). Cingulate cell discharge patterns related to hippocampal EEG and their modulation by muscarinic and nicotinic agents. Brain Res. *460*, 329–338.

Constantinidis, C., and Goldman-Rakic, P.S. (2002). Correlated discharges among putative pyramidal neurons and interneurons in the primate prefrontal cortex. J. Neurophysiol. *88*, 3487–3497.

Csicsvari, J., Hirase, H., Czurko, A., Mamiya, A., and Buzsáki, G. (1999). Oscillatory coupling of hippocampal pyramidal cells and interneurons in the behaving rat. J. Neurosci. *19*, 274–287.

Csicsvari, J., Jamieson, B., Wise, K.D., and Buzsáki, G. (2003). Mechanisms of gamma oscillations in the hippocampus of the behaving rat. Neuron *37*, 311–322.

Dehaene, S., Sergent, C., and Changeux, J.P. (2003). A neuronal network model linking subjective reports and objective physiological data during conscious perception. Proc. Natl. Acad. Sci. USA *100*, 8520–8525.

Destexhe, A., and Sejnowski, T. (2001). Thalamocortical Assemblies—How Ion Channels, Single Neurons and Large-Scale Networks Organize Sleep Oscillations (Oxford: Oxford University Press).

Edwards, E., Soltani, M., Deouell, L.Y., Berger, M.S., and Knight, R.T. (2005). High gamma activity in response to deviant auditory stimuli recorded directly from human cortex. J. Neurophysiol. *94*, 4269–4280.

Engel, A.K., Fries, P., and Singer, W. (2001). Dynamic predictions: oscillations and synchrony in top-down processing. Nat. Rev. Neurosci. *2*, 704–716.

Flint, A.C., and Connors, B.W. (1996). Two types of network oscillations in neocortex mediated by distinct glutamate receptor subtypes and neuronal populations. J. Neurophysiol. *75*, 951–957.

Freund, T.F., and Buzsáki, G. (1996). Interneurons of the hippocampus. Hippocampus *6*, 347–470.

Fries, P. (2005). A mechanism for cognitive dynamics. Neuronal communication through neuronal coherence. Trends Cogn Sci. *9*, 474–480.

Gerbrandt, L.K., Lawrence, J.C., Eckardt, M.J., and Lloyd, R.L. (1978). Origin of the neocortically monitored theta rhythm in the curarized rat. Electroencephalogr. Clin. Neurophysiol. *45*, 454–467.

Gevins, A.S., Zeitlin, G.M., Doyle, J.C., Yingling, C.D., Schaffer, R.E., Callaway, E., and Yeager, C.L. (1979). Electroencephalogram correlates of higher cortical functions. Science *203*, 665–668.

Gibson, J.R., Beierlein, M., and Connors, B.W. (1999). Two networks of electrically coupled inhibitory neurons in neocortex. Nature *402*, 75–79.

Grastyán, E., Lissák, K., Madarász, I., and Donhoffer, H. (1959). The hippocampal electrical activity during the development of conditioned reflexes. Electroencephalogr. Clin. Neurophysiol. *11*, 409–430.

Gray, C.M., and Singer, W. (1989). Stimulus-specific neuronal oscillations in orientation columns of cat visual cortex. Proc. Natl. Acad. Sci. USA *86*, 1698–1702.

Green, J.D., and Arduni, A.A. (1954). Hippocampal electrical activity in arousal. J. Neurophysiol. *17*, 533–557.

Groenewegen, H.J., and Uylings, H.B. (2000). The prefrontal cortex and the integration of sensory, limbic and autonomic information. Prog. Brain Res. *126*, 3–28.

Gutfreund, Y., Yarom, Y., and Segev, I. (1995). Subthreshold oscillations and resonant frequency in guinea-pig cortical neurons: physiology and modelling. J. Physiol. *483*, 621–640.

Harris, K.D., Csicsvari, J., Hirase, H., Dragoi, G., and Buzsáki, G. (2003). Organization of cell assemblies in the hippocampus. Nature *424*, 552–556.

Hasenstaub, A., Shu, Y., Haider, B., Kraushaar, U., Duque, A., and Mccormick, D.A. (2005). Inhibitory postsynaptic potentials carry synchronized frequency information in active cortical networks. Neuron *47*, 423–435.

Holscher, C., Anwyl, R., and Rowan, M.J. (1997). Stimulation on the positive phase of hippocampal theta rhythm induces long-term potentiation that can be depotentiated by stimulation on the negative phase in area CA1 in vivo. J. Neurosci. *17*, 6470–6477.

Holsheimer, J. (1982). Generation of theta activity (RSA) in the cingulate cortex of the rat. Exp. Brain Res. *47*, 309–312.

Howard, M.W., Rizzuto, D.S., Caplan, J.B., Madsen, J.R., Lisman, J., Aschenbrenner-Scheibe, R., Schulze-Bonhage, A., and Kahana, M.J. (2003). Gamma oscillations correlate with working memory load in humans. Cereb. Cortex *13*, 1369–1374.

Huerta, P.T., and Lisman, J.E. (1996). Low-frequency stimulation at the troughs of theta-oscillation induces long-term depression of previously potentiated CA1 synapses. J. Neurophysiol. *75*, 877–884.

Hyman, J.M., Wyble, B.P., Goyal, V., Rossi, C.A., and Hasselmo, M.E. (2003). Stimulation in hippocampal region CA1 in behaving rats yields long-term potentiation when delivered to the peak of theta and long-term depression when delivered to the trough. J. Neurosci. *23*, 11725–11731.

Hyman, J.M., Zilli, E.A., Paley, A.M., and Hasselmo, M.E. (2005). Medial prefrontal cortex cells show dynamic modulation with the hippocampal theta rhythm dependent on behavior. Hippocampus *15*, 739–749.

Ishii, R., Shinosaki, K., Ukai, S., Inouye, T., Ishihara, T., Yoshimine, T., Hirabuki, N., Asada, H., Kihara, T., Robinson, S.E., and Takeda, M. (1999). Medial prefrontal cortex generates frontal midline theta rhythm. Neuroreport *10*, 675–679.

Isomura, Y., Sirota, A., Ozen, S., Montgomery, S., Mizuseki, K., Henze, D.A., and Buzsáki, G. (2006). Integration and segregation of activity in entorhinal-hippocampal subregions by neocortical slow oscillations. Neuron *52*, 871–882.

Jacobs, J., Kahana, M.J., Ekstrom, A.D., and Fried, I. (2007). Brain oscillations control timing of single-neuron activity in humans. J. Neurosci. *27*, 3839–3844.

Jinno, S., Klausberger, T., Marton, L.F., Dalezios, Y., Roberts, J.D., Fuentealba, P., Bushong, E.A., Henze, D., Buzsáki, G., and Somogyi, P. (2007). Neuronal diversity in gabaergic long-range projections from the hippocampus. J. Neurosci. *27*, 8790–8804.

Jones, M.W., and Wilson, M.A. (2005). Theta rhythms coordinate hippocampal-prefrontal interactions in a spatial memory task. PLoS Biol. *3*, e402. 10.1371/journal.pbio.0030402.

Jouvet, M. (1969). Biogenic amines and the states of sleep. Science *163*, 32–41.

Kahana, M.J., Sekuler, R., Caplan, J.B., Kirschen, M., and Madsen, J.R. (1999). Human theta oscillations exhibit task dependence during virtual maze navigation. Nature *399*, 781–784.

Kocsis, B., and Vertes, R.P. (1994). Characterization of neurons of the supramammillary nucleus and mammillary body that discharge rhythmically with the hippocampal theta rhythm in the rat. J. Neurosci. *14*, 7040–7052.

Konopacki, J., Bland, B.H., Maciver, M.B., and Roth, S.H. (1987). Cholinergic theta rhythm in transected hippocampal slices: independent CA1 and dentate generators. Brain Res. *436*, 217–222.

Lakatos, P., Shah, A.S., Knuth, K.H., Ulbert, I., Karmos, G., and Schroeder, C.E. (2005). An oscillatory hierarchy controlling neuronal excitability and stimulus processing in the auditory cortex. J. Neurophysiol. *94*, 1904–1911.

Lee, M.G., Hassani, O.K., Alonso, A., and Jones, B.E. (2005). Cholinergic basal forebrain neurons burst with theta during waking and paradoxical sleep. J. Neurosci. *25*, 4365–4369.

Leung, L.W., and Borst, J.G. (1987). Electrical activity of the cingulate cortex. I. Generating mechanisms and relations to behavior. Brain Res. *407*, 68–80.

Lin, S.C., Gervasoni, D., and Nicolelis, M.A. (2006). Fast modulation of prefrontal cortex activity by basal forebrain noncholinergic neuronal ensembles. J. Neurophysiol. *96*, 3209–3219.

Logothetis, N.K., Kayser, C., and Oeltermann, A. (2007). In vivo measurement of cortical impedance spectrum in monkeys: implications for signal propagation. Neuron *55*, 809–823.

Macrides, F., Eichenbaum, H.B., and Forbes, W.B. (1982). Temporal relationship between sniffing and the limbic theta rhythm during odor discrimination reversal learning. J. Neurosci. *2*, 1705–1717.

Markram, H. (2006). The blue brain project. Nat. Rev. Neurosci. *7*, 153–160.

Menon, V., Freeman, W.J., Cutillo, B.A., Desmond, J.E., Ward, M.F., Bressler, S.L., Laxer, K.D., Barbaro, N., and Gevins, A.S. (1996). Spatio-temporal correlations in human gamma band electrocorticograms. Electroencephalogr. Clin. Neurophysiol. *98*, 89–102.

Miller, R. (1991). Cortico-Hippocampal Interplay (New York: Springer-Verlag).

Montgomery, S.M., and Buzsáki, G. (2007). Gamma oscillations dynamically couple hippocampal CA3 and CA1 regions during memory task performance. Proc. Natl. Acad. Sci. USA *104*, 14495–14500.

Mormann, F., Fell, J., Axmacher, N., Weber, B., Lehnertz, K., Elger, C.E., and Fernandez, G. (2005). Phase/amplitude reset and theta-gamma interaction in the human medial temporal lobe during a continuous word recognition memory task. Hippocampus *15*, 890–900.

Muir, G.M., and Bilkey, D.K. (1998). Synchronous modulation of perirhinal cortex neuronal activity during cholinergically mediated (type II) hippocampal theta. Hippocampus *8*, 526–532.

O'Keefe, J., and Burgess, N. (2005). Dual phase and rate coding in hippocampal place cells: theoretical significance and relationship to entorhinal grid cells. Hippocampus *15*, 853–866.

O'Keefe, J., and Recce, M.L. (1993). Phase relationship between hippocampal place units and the EEG theta rhythm. Hippocampus *3*, 317–330.

Paré, D., and Gaudreau, H. (1996). Projection cells and interneurons of the lateral and basolateral amygdala. Distinct firing patterns and differential relation to theta and delta rhythms in conscious cats. J. Neurosci. *16*, 3334–3350.

Pesaran, B., Pezaris, J.S., Sahani, M., Mitra, P.P., and Andersen, R.A. (2002). Temporal structure in neuronal activity during working memory in macaque parietal cortex. Nat. Neurosci. *5*, 805–811.

Petsche, H., Stumpf, C., and Gogolak, G. (1962). The significance of the rabbit's septum as a relay station between the midbrain and the hippocampus. I. The control of hippocampus arousal activity by the septum cells. Electroencephalogr. Clin. Neurophysiol. *14*, 202–211.

Raghavachari, S., Kahana, M.J., Rizzuto, D.S., Caplan, J.B., Kirschen, M.P., Bourgeois, B., Madsen, J.R., and Lisman, J.E. (2001). Gating of human theta oscillations by a working memory task. J. Neurosci. *21*, 3175–3183.

Rizzuto, D.S., Madsen, J.R., Bromfield, E.B., Schulze-Bonhage, A., Seelig, D., Aschenbrenner-Scheibe, R., and Kahana, M.J. (2003). Reset of human neocortical oscillations during a working memory task. Proc. Natl. Acad. Sci. USA *100*, 7931–7936.

Schoffelen, J.M., Oostenveld, R., and Fries, P. (2005). Neuronal coherence as a mechanism of effective corticospinal interaction. Science *308*, 111–113.

Sederberg, P.B., Kahana, M.J., Howard, M.W., Donner, E.J., and Madsen, J.R. (2003). Theta and gamma oscillations during encoding predict subsequent recall. J. Neurosci. *23*, 10809–10814.

Semba, K., and Komisaruk, B.R. (1978). Phase of the theta wave in relation to different limb movements in awake rats. Electroencephalogr. Clin. Neurophysiol. *44*, 61–71.

Siapas, A.G., Lubenov, E.V., and Wilson, M.A. (2005). Prefrontal phase locking to hippocampal theta oscillations. Neuron *46*, 141–151.

Silva, L.R., Amitai, Y., and Connors, B.W. (1991). Intrinsic oscillations of neocortex generated by layer 5 pyramidal neurons. Science *251*, 432–435.

Sirota, A., and Buzsáki, G. (2007). Interaction between neocortical and hippocampal networks via slow oscillations. Thalamus Relat. Syst. *3*, 245–259.

Sirota, A., Csicsvari, J., Buhl, D., and Buzsáki, G. (2003). Communication between neocortex and hippocampus during sleep in rodents. Proc. Natl. Acad. Sci. USA *100*, 2065–2069.

Somogyi, P., and Klausberger, T. (2005). Defined types of cortical interneurone structure space and spike timing in the hippocampus. J. Physiol. *562*, 9–26.

Steriade, M., and Amzica, F. (1996). Intracortical and corticothalamic coherency of fast spontaneous oscillations. Proc. Natl. Acad. Sci. USA *93*, 2533–2538.

Sukov, W., and Barth, D.S. (1998). Three-dimensional analysis of spontaneous and thalamically evoked gamma oscillations in auditory cortex. J. Neurophysiol. *79*, 2875–2884.

Swanson, L.W. (1981). A direct projection from ammon's horn to prefrontal cortex in the rat. Brain Res. *217*, 150–154.

Swanson, L.W., and Kohler, C. (1986). Anatomical evidence for direct projections from the entorhinal area to the entire cortical mantle in the rat. J. Neurosci. *6*, 3010–3023.

Thierry, A.M., Gioanni, Y., Degenetais, E., and Glowinski, J. (2000). Hippocampo-prefrontal cortex pathway: anatomical and electrophysiological characteristics. Hippocampus *10*, 411–419.

Tierney, P.L., Degenetais, E., Thierry, A.M., Glowinski, J., and Gioanni, Y. (2004). Influence of the hippocampus on interneurons of the rat prefrontal cortex. Eur. J. Neurosci. *20*, 514–524.

Ulrich, D. (2002). Dendritic resonance in rat neocortical pyramidal cells. J. Neurophysiol. *87*, 2753–2759.

Vanderwolf, C.H. (1969). Hippocampal electrical activity and voluntary movement in the rat. Electroencephalogr. Clin. Neurophysiol. *26*, 407–418.

Varela, F., Lachaux, J.P., Rodriguez, E., and Martinerie, J. (2001). The brainweb: phase synchronization and large-scale integration. Nat. Rev. Neurosci. *2*, 229–239.

Vertes, R.P., Albo, Z., and Viana, D.P. (2001). Theta-rhythmically firing neurons in the anterior thalamus: implications for mnemonic functions of Papez's circuit. Neuroscience *104*, 619–625.

Witter, M.P. (1993). Organization of the entorhinal-hippocampal system: a review of current anatomical data. Hippocampus *3 Spec No*, 33–44.

Womelsdorf, T., Schoffelen, J.M., Oostenveld, R., Singer, W., Desimone, R., Engel, A.K., and Fries, P. (2007). Modulation of neuronal interactions through neuronal synchronization. Science *316*, 1609–1612.

Wyart, V., and Tallon-Baudry, C. (2008). Neural dissociation between visual awareness and spatial attention. J. Neurosci. *28*, 2667–2679.

Neuron, Volume *60*

Supplemental Data

Entrainment of Neocortical Neurons and Gamma Oscillations by the Hippocampal Theta Rhythm

Anton Sirota, Sean Montgomery, Shigeyoshi Fujisawa, Yoshikazu Isomura, Michael Zugaro, and György Buzsáki

Supplemental Experimental Procedures

Chronic Animal Surgery

For chronic experiments, 28 Long Evans rats (male, 250-400 g) and 11 mice (male, 30-40 g) were deeply anesthetized with isoflurane or ketamine/xylazine. Details of surgery and recovery procedures have been described earlier (Csicsvari et al., 2003). Various electrodes were implanted for unit and LFP recording. All rats and mice were implanted with a microdrive that allowed the positioning of recording electrodes. In 13 rats, linear silicon probes (NeuroNexus Technologies,16 recording sites at 100 µm vertical spacing) were implanted in somatosensory/parietal cortex and the CA1 pyramidal layer of the dorsal hippocampus (Sirota et al, 2003). In one rat, a single shank linear silicon probe was implanted in the medial prefrontal cortex. In four rats, high density 8-shank 'octrode' (15 µm spacing), 64-site probes, (Bartho et al., 2004) were implanted in the medial prefrontal cortex (AP 3.0-4.4, ML 0.5) and posterior hippocampus. In 3 rats, 6-shank, 96-site linear probes were implanted in the parietal cortex in the right hemisphere parallel to the transverse axis of the hippocampus (45^{o} parasagittal) with the outer shanks targeted at approximately (AP -2.8, ML 2.7), and (AP -3.86, ML 1.64) with tips in the CA1 pyramidal layer of the dorsal hippocampus (Montgomery and Buzsaki, 2007). The position of the electrodes was confirmed histologically. In 4 rats and 11 mice 2 to 8 independently movable wire tetrodes were implanted in the parietal cortex and hippocampus (Sirota et al., 2003; Zugaro et al., 2005). In all chronic experiments ground and reference screws were implanted in the bone above the cerebellum.

Chronic Animal Behavior

Four rats with electrodes implanted in prefrontal cortex were trained in a working memory task (spontaneous alternation task or odor-based delayed matching-to-sample task in a figure 8-shape maze). The remaining rats were trained to run on a linear track for water reward (Zugaro et al., 2005). In addition, the animals were recorded during sleep in the home cage. Spectral features of the LFP were used to segment the recording session into periods of REM sleep and awake running ("theta-associated behaviors"; Figure S1). Analysis was performed on 95 REM sessions and 34 waking run sessions. In 27 cases, data from the same set of neurons was recorded during both REM and waking sessions.

Acute Experiments
Experimental details for the acute experiments, along with other data from the same animals, have been published (Isomura et al., 2006).

Data Acquisition and Processing
Extracellular signals were amplified and filtered by multi-channel AC amplifiers (Sensorium EPA5 or RC Electronics; 1000x; 1 Hz to 5 kHz). The intracellular signals were amplified with a DC amplifier (Axoprobe 1A; Axon Instruments). Wide-band extracellular and intracellular signals were digitized at 20 kHz sampling rate with 16-bit resolution and stored for offline analysis using one or two synchronized 64-channel DataMax Systems (RC Electronics, Santa Barbara, CA, USA). Raw data were preprocessed using a custom-developed suite of programs (Csicsvari et al., 1999). The wide-band signal was downsampled to 1.25 kHz and used as the local field potential signal. For spike detection, the wide-band signal was high-pass filtered (>0.8 kHz). Single units were isolated semi-automatically by a custom-developed clustering analysis program KlustaKwik (http://klustawik.sourceforge.net) (Harris et al., 2000) and refined manually using custom-made software (http://klusters.sourceforge.net; http://neuroscope.sourceforge.net; Hazan et al., 2006). For tracking the position of the animals, two small light-emitting diodes, mounted above the headstage, were recorded by a digital video camera and sampled at 30 Hz. Malfunctioning recording sites (e.g., due to high impedance, cross-talk or short circuit) were removed from the analysis (shown in gray in the plots in Figures 3,4,5,6 and 8). Current-source density (CSD) was calculated using a robust second derivative approximation scheme (Freeman and Nicholson, 1975). Spatial smoothing with a triangular kernel was applied to remove spatial noise that stemmed from the variability of electrode impedances.

Data Analysis
LFP, extracellular unit activity and intracellular data were analyzed, unless stated otherwise, by custom-written, MATLAB-based programs. Processing was done either on a stand-alone Linux server or using a Linux cluster (ravana.rutgers.edu; the authors thank Yaroslav Halchenko, Department of Psychology, Rutgers University, for professional cluster administration).

Monosynaptic Connections
For the identification of excitatory and inhibitory connections between neurons, short-latency, short-duration sharp peaks/troughs in the cross-correlograms were used (Bartho et al., 2004;Constantinidis et al., 2001;Csicsvari et al., 1998). Monosynaptic connections between pairs of units were detected using a custom-made interactive software followed by a non-parametric significance test based on jittering of spike trains for computation of the global significance bands (Fujisawa et al., 2008). Significant peaks ($p<0.01$) within 5 msec of the center bin were considered as putative excitatory monosynaptic connection. Similarly, short-latency troughs were considered to be due to inhibition when at least two neighboring 1 msec bins were significantly depressed. For cell pairs recorded from the same electrode, the 0-1 msec bin was not considered, because our clustering program cannot resolve superimposed spikes.

Cell Type Classification

For each unit, various parameters were calculated, including 1) filtered (0.8 kHz – 5 kHz) spike waveshape parameters: trough to right (late) peak, trough to left (earlier) peak and half amplitude width, asymmetry index (ratio of the difference between right and left baseline-to-peak amplitudes and their sum), 2) firing rate 3) features of the auto-correlogram. Next, we explored the multi-dimensional space formed by these parameters for the subset of units identified as inhibitory or excitatory based on cross-correlogram analysis as described above. The parameters that allowed best separation between the two putative anatomical groups were the trough to right peak latency (related to the repolarization of the intracellular action potential; Henze et al., 2000) and asymmetry index (possibly reflecting differences in the rate of fall of spike repolarization). We used the hyperplain that divided the two physiologically identified classes (interneurons and pyramidal cells) to separate units into putative interneurons and putative pyramidal cells. No attempt was made to distinguish between different types of pyramidal cells or among the large family of interneurons (Markram, 2006;Somogyi et al., 1998). The reliability of our physiological classification method will require anatomical verification of the putative neuron types in future experiments.

Theta Phase Extraction

LFP in CA1 pyramidal layer was filtered with multitaper filter with bandwidth of 1 Hz whose pass-band range was adapted to the instantaneous (within 1 sec window) frequency of theta. Instantaneous theta phase was estimated by Hilbert transformation of the filtered signal. This procedure ensured that prior distribution of phase is uniform (the prior distribution of phases in each session was tested for uniformity prior to unit analysis), since otherwise all circular statistics should be corrected for the bias (Siapas et al., 2005). Although such definition of phase does not take into account waveshape asymmetry, we believe it is a more conservative approach because waveshape asymmetry depends on filter settings, instantaneous theta power and frequency and it varies in time. Nevertheless, we performed all circular statistics tests with non-uniformity bias-correction procedure as described in Siapas et al (2005) and these tests were congruent with our more conservative approach.

Phase Modulation Analysis

First, we used the standard Rayleigh test for uniformity of the phase of unit firing. This test is the most powerful invariant test of uniformity against the von Mises alternative. Rayleigh test is equivalent to a likelihood ratio test, and the statistics of this test $2R^2/n$ (R - resultant length, n - sample size) has an asymptotic chi-square distribution with 2 degrees of freedom (Jammalamadaka and SenGupta, 2001;Mardia and Jupp, 2000). Therefore the appropriate statistics for significance test is $Z=R^2/n$, or variance-stabilized $log(Z)$. Since statistical distribution is only true asymptotically, the size of the sample can also be a factor (for small n). We performed Monte Carlo simulations to test the performance of Rayleigh test for small samples and found that p-values were in very close agreement for even very small sample sizes. Once the sample is rejected (i.e., nonuniform), one must realize that the sample estimate of resultant length R is strongly biased upwards, and this bias increases as the sample size decreases. Therefore, all measures derived from R, such as the mean resultant length (R/n) and maximum

likelihood (ML), estimate of the concentration coefficient of von Mises distribution (k) and $Z = R^2/n$ have a bias, which depends on the sample size if the sample is drawn from a nonuniform circular distribution. Therefore, the use of these parameters as quantifiers of the modulation strength is not appropriate for small samples. We used Monte Carlo simulations to estimate the sample size at which bias in the estimate of R is sufficiently small. We find that for sample size >1000 the bias in the estimate of R can be neglected. Thus, for comparison across cells and conditions we used concentration coefficient k estimated for subpopulation of cells which emitted more than 1000 spikes (Figures S2,9). We used both conventional maximum likelihood estimate of k and maximal marginal likelihood estimate (Schou, 1978), which has much lower bias for small sample sizes. Both estimates agreed well for sample sizes above 1000.

Another issue in this context is the alternative model of Rayleigh test, the von Mises distribution. This is an important consideration because phase-modulation of unit firing may not follow von Mises distribution, e.g., it could be skewed or multimodal. Thus, the Rayleigh test for uniformity is biased to a degree at which the alternative is not von Mises type, and can be biased depending on cell firing pattern and state. This will also affect the dependence of R and measures derived from it on the sample size. To alleviate some of these issues, we performed additional tests: nonparametric goodness-of-fit Kuiper's and Watson's U^2 tests (Jammalamadaka and SenGupta, 2001;Mardia and Jupp, 2000), which test for uniformity against any alternative. Both tests statistics were correlated with Rayleigh logZ ($r>0.9$, $p<0.00001$), suggesting that model choice was not a determinant factor (Figure S2). Finally, we computed bootstrap Rayleigh tests by subsampling each sample 500 times with a subsample of size 100, which allowed ruling out the effect of sample size on the Rayleigh statistics. This approach, however, is dramatically reducing the power of the test for cells with high sample size. To this end, we have no rigorous resolution for this problem.

Variations in the sample size and contamination of spike train, and therefore a bias on the estimates of R, could arise from imperfect spike sorting. We tested for systematic correlation between the Rayleigh statistic log$Z$ and cluster quality measure (eDist (Harris et al., 2000)). Cleaner clusters tended to be associated with stronger modulation of putative interneurons ($r=0.21$, $p<10^{-5}$), whereas for pyramidal cells there was no such trend ($r=-0.001$, $p=0.45$). This could be explained by the generally smaller amplitude of interneurons and their stronger contamination by noise (including multiple unit activity of more distant neuronal populations and instrumentation noise). Noise-contaminated clusters effectively decrease theta phase-modulation because non-biological noise is independent of theta phase and firing of other neurons may have different phases than the clustered neuron. In summary, noise contamination may have underestimated the degree and percentage of significantly modulated interneurons, but it did not affect the results for putative pyramidal cells.

Coherence analysis between hippocampal LFP and neocortical spike trains provided a frequency resolved measure of theta modulation of spiking activity in the neocortex (Figure S3) and was, in general, comparable to circular statistics.

The significance of theta modulation can be assessed by using binomial distribution for the number of rejections of uniformity hypothesis at any given alpha level. For example, for pyramidal cells in the parietal cortex the number of rejections of uniformity at alpha=0.05 was 12%, whereas the expected chance level is 5%. The significance of the excess of the number of rejections is determined by the probability to observe 12% (K=63 cells), given the null distribution (binomial with p=0.05 and N=522). This result is very significant (from the binomial distribution we obtain p-value$<10^{-10}$; using normal approximation of binomial distribution we obtain Z-score of observed number of rejections 7.4). Similarly, for alpha=0.01, the observed rejection percentage is 4%, which yields p-value$<10^{-34}$, z-score =9.1; for alpha=0.001 z-score=17.4. It is clear from Figure 2E that as alpha is decreasing the excess of rejections beyond chance is becoming increasingly significant. For example, there were 9 pyramidal cells (1.7%) with p-values <0.0001; this corresponds to the z-score of ~39!

Mixture Model Fit

For a subset of significantly nonuniformly modulated neurons we tested whether their spike phase distribution is better described by Von Mises distribution, or a more general model, a mixture of Von Mises and circular uniform distributions. The procedure was as follows:

Step 1: Test for uniformity against von Mises alternative (Rayleigh test)
Step 2: If uniform is an adequate model ($p > 0.05$), analysis was discontinued.
Step 3: Otherwise, test for "von Misesness" against the mixture alternative using likelihood ratio test
Step 4: If von Mises model is adequate, the analysis was terminated and the von Mises model was used. Goodness of fit test was performed based on Watson's U^2 statistic.
Step 5: Otherwise test the fit of mixture model (using goodness of fit test based on Watson's U^2 statistic; we did not consider models more complex than the mixture model)
Step 6: If mixture model was adequate, then the mixture model was used.

The above-mentioned sequence of tests was performed using a code in R language provided by John Bentley (Bentley et al., 2007). For ~11% of neurons the likelihood ratio test argued in favor of the mixture model. For the remaining neurons a simpler model (von Mises) provided an adequate fit. Because the firing of every neuron is driven presumably by a combination of phase-related and phase-independent inputs, a mixture model may be more accurate from the physiological point of view for the description of phase-modulation.

Spectral Analysis

Unit and LFP power spectrum and unit-unit, unit-LFP, and LFP-LFP coherence estimates were performed using multitaper direct spectral estimates. For theta frequency range, we typically used window sizes of 1-2 seconds and 3-5 tapers, and for gamma range – 50-200 msec and 5-9 tapers. Estimates that involved units were made only on windows that contain at least as many spikes as tapers used (Jarvis and Mitra, 2001). For coherence estimates we verified homogeneity assumption in a selected set of data by comparing the error bars computed by jackknife and theoretical estimate.

Spatial localization of gamma coherence requires, strictly speaking, multiple comparison tests for testing significance. Due to clear topographic localization of LFP with significant peaks at the same gamma frequency, we are confident that most permutation tests would show a significant effect.

In addition to coherence estimates, we also performed phase-locking index estimation (equivalent to Rayleigh test for each frequency bin) and power correlation. These two measures are combined in the coherence measure due to nonstationarity of power across windows. Invariably, increase in coherence at a certain frequency and location was associated with increased phase-locking at the same frequency and location.

Unit-triggered average spectrum was computed in 200-msec windows at different time lags from the time of spike for every recording site. The "baseline" spectrum calculated for the entire session was subtracted from the unit-triggered spectrum for spatial localization analysis to estimate the deviation of the spectrum during unit firing from the overall mean. In some cases, increase in absolute gamma power was more prominent in the hippocampus than at neocortical sites. This could reflect a non-Poisson and nonwhite statistics of unit firing and gamma power. Unit-triggered average spectrum is equivalent to a correlation coefficient between the binary process of unit firing and gamma power at every frequency bin. As such, it is not known whether both unit firing and gamma power are co-modulated by hippocampal theta. In the frequency domain, the cross-correlogram is equivalent to cross-spectrum, which contains both amplitude correlation and phase-locking between the two signals. In our analysis the primary goal is to reveal neocortical gamma sources associated with unit firing. Therefore, power spectra of unit firing and gamma power may confound the strength of the phase relationship between unit activity and gamma oscillations– the goal of the analysis. Moreover, for different recording sites the magnitude of gamma power modulation by theta phase may vary. Finally, volume conduction of LFP is a further potential confound. Due to these considerations, unit-triggered spectral analysis is adequate only for neurons that are not very strongly modulated by hippocampal theta and can be reliably associated with a single gamma source.

Theta Modulation of Gamma Power

The predictable effects of volume-conduction can be exploited in some special cases to support our general conclusion regarding the hippocampal theta modulation of neocortical gamma oscillations. High frequency gamma (>100 Hz) was well defined in the neocortex but weaker in the hippocampus. Importantly, there was a clear gap in the spatial profile of power in the high gamma band between neocortical locations and the hippocampus (not shown), an convincing argument against volume conduction of hippocampal gamma to the neocortex, at least for higher frequencies. We estimated gamma power at all cortical locations in short (50-100 msec), temporally overlapping sliding windows and determined the magnitude of theta modulation of the resulting signal at every gamma frequency bin by calculating the coherence between LFP in the CA1 pyramidal layer and gamma power time series in the respective frequency bin.

Local Maxima of Gamma Power

To detect isolated gamma bursts in the neocortex, we limited our analysis to gamma bursts, which were localized in space, frequency and time and were sufficiently well isolated in these dimensions from other gamma bursts. These events were identified as local maxima in the 4-dimensional (time x frequency x shank number x site number) matrix of spectral power (Figure 4D). This constraint allowed the segregation of gamma bursts in terms of their spatial and frequency localization and the examination of their theta modulation. Although this approach limits the analysis to gamma bursts with no contiguity in any dimension to other gamma bursts, it avoids the problem of linear mixing of different gamma sources. Using this approach, were obtained suffiently large numbers of gamma bursts in many of our datasets. The local maxima of these gamma bursts demonstrated a clear nonrandom clustering in space (Figure 4F) and frequency. Because frequency had a clear bimodal distribution (Figure 4E), we divided gamma bursts into fast and slow (above and below 100 Hz) events. This classification yielded 5-15 clusters in a dataset, each with localized spatial and frequency properties. The time of occurrence of gamma bursts from individual clusters was then used in the theta phase modulation analysis.

Gamma Frequency-Location (gFL) Factor Analysis

gFL factor analysis consists of the following steps:

1. Whiten the LFP from all recording sites. Perform autoregressive model of the second order with coefficients vector A that fit to the data. This low order model essentially fits the "pink" shape of the spectrum (~1/f). Then a filter [1; -A] is used to filter the LFP signal to remove the pink component. Whitening essentially equalizes the variance across frequency bins and decreases frequency leakage during spectral estimates. The same whitening model is used for all sites.
2. Compute spectrum of whitened LFP for each site in the range of 30-150 Hz for overlapping 100 msec windows stepping by 13 msec (steps of 20, 50 and non-overlapping windows were also tried and did not yield different results, but reduced the temporal resolution of the method needed for analysis) that cover all robust theta epochs (during REM or RUN session). As a result we obtain nCh matrices of size nVariables = nF * nT, where nCh – number of sites, nF – number of frequency bins, nT – number of time bins.
3. Log-transform the matrices to bring marginal distributions for each variable (frequency bin on one channel) to a more symmetric form (closer to normal). Concatenate spectral matrices along frequency dimension to form a matrix M of size (nF*nCh) x nT. Here nF*nCh – number of variables for future multivariate analysis and nT – number of samples.
4. Perform PCA on matrix M, leave 99.9% of the variance in the model. This gives a matrix of principal component eigenvectors W. Since gFL analysis concerns only the small subspace (spanned by ~30) eigenvectors, corresponding do largest eigenvalues, the amount of data (nT/nVariables ratio was between 10 and 100) were large compared with the size of this subspace,and the subspace was well populated by data.
5. Perform orthogonal rotation of the matrix W using the Varimax method (Kayser and Tenke, 2003;Reyment and Joreskog, 1993), employing simplicity criteria to

obtain a matrix of factor loadings. The goal of simplicity criteria is to obtain factors with only a few high loadings and near-zero loadings for the majority of variables. Such rotation turns factors from simply spanning the directions of largest variance, which are not physically meaningful, into factors that capture a parsimonious structure in the covariance matrix and is more likely to be physiologically meaningful. In short, the essence of the method is this: rotated factors will correspond to the directions in the spectral space, which span limited frequency bins at a few sites with strong covariance. Another benefit of the method is that factor loadings are always non-negative, thus it eliminates the ambiguity of the sign of the factor loadings present in PCA.

6. Compute variance explained by rotated factors, factor scores – projection of the data on the rotated factors.
7. For further analysis, we computed only the first 30 factors because the first 5-20 factors explained most of the variance. This procedure is likely to result in an underestimation of the true number of factors. Factors that had high loadings on only 1 or 2 frequency bins or 1 or 2 dispersed sites were considered artifacts and removed from the analysis. Factors with maximal loadings on the boundary frequency bins stem from spectral leakage from lower or high frequency ranges and were also removed.
8. We further determine the location of the maximum loading of each factor in frequency and location. The latter is estimated as the center of mass in anatomical space covered by the recording sites. Most factors produced highest loadings concentrated around one frequency bin and one anatomical location. Frequency and location of the gFL were typically independent of each other. Therefore, for each factor we compressed the nF x nCh vector of factor loadings (Figure 4D) into two vectors (profiles) – Frequency profile (factor loading across all frequency bins at maximal loading location) and Location profile (factor loading across all sites at the maximal loading frequency bin). Factors were classified as neocortical or hippocampal depending on the anatomical location of the maximal loading.
9. Factor scores were computed by projecting the original spectral matrix on the factor loading vector. To reduce the contribution of the gamma power away from the gFL center we set the factor loading values to zero for all elements with loading below 15 percentile. In mathematical notation, if X is original data matrix, A is a matrix of factor loadings and S is a matrix of scores, we are seeking decomposition $X=A*S+e$, where e is an error term. To obtain the score matrix given a matrix A ("project" the data X on A) we computed the pseudo-inverse of A and multiplied it with the data matrix X: $S=A^{-1}*(X-e)$. Time series of the factor score represents the change of weight of the factor across time. Thus, this continuous variable can be interpreted as the "strength" of gamma oscillation characterized by both Frequency profile and Location profile (gFL). Coherence between gFL score and LFP was performed using multitaper estimates as described above. LFP signal was resampled at time stamps centered on the spectral windows used to compute the spectrograms (see step 2).
10. Peaks of gFL scores are detected as local maxima separated by at least 50 msec and above 75 percentile of the overall score distribution. Peak times represent the occurrence of the gamma "burst" characterized by Frequency and Location

profiles. Circular statistic analysis was performed on theta phase at the time of gamma bursts for each gFL. We found no correlation between the Rayleigh statistic logZ and variance explained by the gFL factor (r~-0.06), indicating that gamma bursts were theta modulated independent of how prominent they were.

Partial Coherence Analysis

Since projection of the large gamma power from sites with small loadings (hippocampal sites) can still bias the gFL score due to possible volume conduction from hippocampal sites, we computed partial coherence between the neocortical gFL score and LFP by partializing it by the gamma power in CA1 pyramidal layer, filtered according to the frequency profile of the respective gFL. Partial coherence was considered non-significant if its values at theta frequency band fell below the significance level determined from full coherence. Clearly, the larger the power of hippocampal gamma, the stronger the effect of volume conduction to the neocortex, but the converse is also true – the larger the power of neocortical gamma (which is the case for low frequencies), the more it contributes to gamma power measured in CA1 pyramidal layer. This may result in significant decrease of partial coherence value – false negative result.

Theta Modulation of LFP-LFP Gamma Coherence

A limitation of gFL factor analysis is that it is based the spectral power, which limits one's ability to perform linear unmixing of the individual gamma oscillators. Addition of phase information to the analysis would strongly improve the method, but requires further improvement of this method, a goal which lies beyond the scope of this paper. Importantly, the gFL analysis should be considered as an effective exploratory tool to identify the location and frequency of individual gamma oscillators but it must be validated by spectral analysis which includes phase information of the signal.

For each gFL we validated the analysis in the following way. We computed coherence between the LFP in the center of the gFL-identified spatial gamma profile (center of mass of spatial factor loading) and the LFP at all other recording sites. We used spectral windows of 50 msec and 9 tapers. The average coherence over the entire session typically had a significant peak at the frequency close to preferred frequency of the gFL and had spatial profile at this frequency that matched that of the gFL in question (Figure 6J), providing a phase-synchronization measure of the local neocortical gamma. Analysis of the spatial coherence maps allowed us to determine the presence or absence of local oscillations. If no local oscillations are found in the center of gFL, presumably due to volume conduction from elsewhere (e.g., from hippocampus), the coherence between the center and the location of source of gamma currents (local-distant) is expected to be higher than between the center and nearby locations (local-local). Thus, in case of volume conduction the spatial profile of coherence at gamma frequency would have a maximum away from gFL center. Since there are always some locally generated currents, albeit with flat (white or pink) spectrum, the local-local coherence across all the frequencies may be higher than that of local vs. distant. However, this would be true for any frequency bin. In short, presence of high coherence in a narrow frequency band spatially confined to the center of gFL can be considered as evidence for locally generated gamma.

To test whether hippocampal theta modulates neocortical gamma, we can use the spatial profile of gamma band coherence as a measure of local gamma synchronization. The logic behind this approach is as follows. Let us assume that there are two gamma oscillators (local-neocortical and distant-hippocampal), the power of the local one is not modulated by theta, whereas the power of the distant one is modulated. Then, on average, local-local coherence is maximum around the center of neocortical gamma in a frequency band of neocortical gamma. Now we can compute the gamma band coherence in short moving windows and quantify the coherence of these time series to the theta LFP in hippocampus ('coherence of gamma coherence' measure). The temporal fluctuation of the local-local coherence is coherent with theta oscillations since both local sites at the gamma source detect the volume-conducted signal from the distant theta modulated gamma source, but the coherence of the fluctuation of local-distant gamma band coherence with theta must be stronger, because it is less contaminated by non-theta related local gamma. Thus, the spatial profile of the coherence of gamma band coherence fluctuation to theta (i.e., theta modulation of gamma synchrony) should have a maximum at the source location of theta modulated gamma, and not locally. If, on the other hand, the local neocortical gamma is modulated by theta, we should expect to see maximum coherence of gamma coherence fluctuations to theta at the center of neocortical gamma oscillator. To quantify this relationship, we computed the integrated LFP-LFP coherence within the preferred gFL frequency band in short running windows (50-100 msec) for the entire session, and estimated the coherence between this time series and hippocampal LFP for each pair of all recording sites. We determined the similarity between the spatial profile of the coherence of gamma coherence to the spatial profile of average gamma coherence and the gFL spatial profile in all sessions recorded with 96-site silicon probes, which provide 2^d spatial coverage of both neocortex and underlying hippocampus. In only a few cases we found that maximal coherence of gamma coherence was localized away from the center of respective gFL, indicating that that theta modulation of gamma oscillation occurred elsewhere in the neocortex, independent of the sample gFL. In most cases, however, gFLs and the coherence profiles strongly overlapped, indicating that the power of local neocortical gamma is theta modulated. Thus the effect of volume conduction from any other gamma sources can thus be ruled out in this analysis (e.g., Figure 6K).

Potential Caveats of the Gamma Analysis

Gammas oscillations in the neocortex are typically transient and small amplitude. Detection and isolation of such small amplitude signals often require high spatial resolution methods and complex mathematical-statistical procedures. Because of such complexities, no straightforward tools can be offered. Below, we address some of the caveats and solutions of the methods used in our analyses.

What Is the Effect of Whitening of the LFP Prior to Spectral Analysis?

There are two main reasons for whitening the signal in our analysis. First, whitening reduces the dynamic range of the signal and thus reduces the leakage of low frequencies into the higher frequency bins during spectrum estimation. This reduces the bias in the spectrum estimation (Pesaran and Mitra, 1998). Second, we wanted the variance at different frequency bins to be the same and their contribution to the covariance matrix

comparable. Whitening adjusts the ~1/f falloff of the spectral power with frequency, which is mostly the consequence of the fact that slower frequencies can synchronize over large spatial domains and result in larger amplitude signals. It is not the exact power of the gamma oscillations in different frequency ranges, but their temporal dynamics, that we aimed to explore, and thus we did want to make their contributions to the covariance matrix independent of their absolute amplitudes. There is no physiological reason to believe that signals of lower power are less important than signals of high power, given that they may have different physiological mechanisms. Covariation between power values at different recording sites and frequency bins reflects the presence of oscillatory source located around these sites with peak power at the corresponding frequency range. In statistical terms, whitening is aimed to standardize the data at different frequency bins before the factor analysis, a standard procedure in multivariate analysis (e.g. Krzanowski: Principles of Multivariate Analysis).

How Do Harmonics of Theta Confound the Analysis?

First, the whitening procedure equally emphasizes theta harmonics and genuine gamma oscillations, hence whitening makes no difference for the gamma range analysis. Second, the maximal power of higher harmonics of theta in the gamma range do not reach, on average, more than ~20% (for 2^{nd}) and ~7% (for 3^{rd}, 32-40 Hz) of the average theta power at the fundamental frequency. Contributions of higher harmonics are much smaller. Therefore, the putative contribution of theta harmonics is limited to the low range of gamma frequency band (<40Hz). In contrast, the strongest theta phase modulation, according to our various analyses (gamma power, gFL and LFP-LFP coherence modulation), was observed at higher frequencies (>100 Hz), which could not stem from higher harmonics of theta oscillations. Furthermore, if theta harmonics artificially generated gFL factors they would have a center of mass in the hippocampus and not in the neocortex. Third, since the power of theta harmonics is independent of the power of true gamma oscillations, individual gFLs that could stem from theta harmonics could be easily identified. During the screening of gFL factors, we removed all factors with maximal loading in the lower frequency bin (30 Hz). Likewise, we did not detect local maxima of spectral power with isolated power below 30 Hz.

Is the Covariance Matrix Well-Conditioned and Does It Affect the gFL Analysis? How Robust Is the Method?

As discussed in the gFL method section, the number of data points was much larger than the number of variables. Due to volume conduction, the covariance matrix cannot be under-populated. Nevertheless, because of putative volume conduction and comodulation of gamma oscillators the covariance matrix suffers from multicollinearity and has high condition number. However, ill-conditioning of the matrix will only surface during the inversion. Neither PCA dimensionality reduction nor the Varimax rotation will be affected by the high condition number of the matrix, because they do not include the covariance matrix inversion. The ill-conditioning of covariance can be reflected in the estimation of the sources for the smallest eigenvectors. In fact, one of the methods to regularize ill-conditioned matrices is based on truncation of smallest eigenvalues in SVD (e.g. P. C. Hansen: Rank-Deficient and Discrete Ill-Posed Problems: Numerical Aspects of Linear Inversion). Furthermore, we constrained the Varimax rotation to the subspace

spanned by the first *r* principal components, where *r* is the number of eigenvalues larger than 10^{-4}. Typically, *r* was slightly smaller than number of variables. Since our analysis uses only highest (typically less than 20) eigenvectors, they will not be affected by ill-conditioned covariance matrix.

In addition, we ran several tests on our data. First, we computed Kaiser-Meyer-Olkin Measure of Sampling Adequacy (Kaiser 1970, 1981), which indicates whether the data factors are well based on correlations and partial correlations between the variables. For all data sets, this statistic was above 0.85 (mean = 0.95, std = 0.02). Random data would correspond to 0.5 and values >0.8 indicate high suitability for factor analysis. It is clear from this analysis that ill-conditioning of the covariance matrix is in fact correlated with its suitability for factor analysis. Second, we split the data in two halves and compared the covariance matrices. To do so we computed single value decomposition and compared the eigenspectra of the covariance matrices for two halves of the data set. The relative difference between eigenvalues was 2%±1.8%, which indicates that we have sufficient amount of data to get consistent estimates of the covariance matrix. Analysis of eigenspectra differences showed consistent increase in the relative eigenvalue difference towards the end of the eigenspectra (i.e. for small eigenvalues), which further supports our contention that the variability/errors in the covariance matrix estimation corresponds to the small eigenvalues, and thus will not affect the PCA or Varimax rotation.

We could not perform a full 10-fold cross-validation due to constraints of sample size, but we did perform the entire gFL analysis in first and second halves of all datasets. We found a close correspondence between the factor loading vectors obtained from full dataset and either half (Figure S9). The consistency between the two halves of data support our conclusions that (a) we had enough data for the proper estimation of the covariance matrix, (b) changes in covariance matrix (first and second half) did not affect the outcome of the analysis, and (c) spatial and frequency profiles were not random or trivial. Equally importantly, the degree of theta modulation of the gFL scores in the first and second halves of data was highly correlated for most of the gFLs, and even the preferred theta phase matched very closely (Figure S9). This means that each gFL score represents the time course of an independent process, which can be theta modulated to a certain degree and at a given preferred phase. This is not expected if any step of the analysis included random (noise, artifact) driven signal. Random noise would not give rise to (a) phase relationship to theta and (b) consistency between the two halves of the datasets. This analysis further argues against the pivotal role of volume-conduction, since volume conduction of hippocampal gamma to different cortical locations would result in *similar* theta modulation strength and phase. We believe this is a strong argument against the alternative that randomness and arbitrariness gave rise to the observed effect in our analyses, and suggests that gFL analysis does perform satisfactory demixing of individual gamma time courses.

Does the Linear Nature of gFL Analysis Introduce Rather Than Alleviate the Problem of Volume Conduction?

Volume conduction results in a linear mixing of different gamma sources. There is no ideal method to perfectly solve this problem. All existing methods are based on linear

transformations. For example, current source density (CSD) method, widely used in neuroscience community, is a linear transformation of voltage values. CSD improves the localization of the current sinks and sources and follows from the Maxwell equations.

First, our analysis was not affected by the imperfections of factor analysis (such as nonzero factor loading in hippocampus for the neocortical gFLs). For each gFL the factors score was calculated by projecting the data on the subspace formed by the sites from the upper 85% of the factor loading values and proximal to the center of gFL. Second, as the goal of linear factorization is to unmix linearly mixed sources. Even though all elements of loading matrix A are nonnegative, some elements of pseudo-inverse A^{-1} are negative, and it is precisely the elements corresponding to gamma frequency bins derived from sites away from the gFL center or preferred frequency (e.g. hippocampal sites) that will be negative. Because of this negative contribution in the linear combination, it alleviates the problem of volume conduction, rather than emphasizes it. Third, the contribution of theta modulated hippocampal gamma to neocortical gamma was also ruled out by the partial coherence analysis. If linear contribution of gamma power at any frequency explained theta modulation of the gFL score, partializing the coherence by the power of hippocampal gamma should abolish the coherence. This was not the case. Fourth, the goal of gFL analysis is exploratory: due to volume-conduction (leading to linear mixing) and variable power of different gamma oscillators it is not possible to determine the location and frequency of gamma oscillators *a priori*. However, factor analysis allows one to uncover the spatial and frequency structure of the diverse arrays of gamma oscillators. This information can be further used to perform more direct analyses (e.g. LFP-LFP coherence) within the uncovered spatial and frequency loci.

Does Current-Source Density Analysis or Local Referencing Eliminate Volume Conduction?

The voltage produced by volume conducting currents decays inversely with distance from the point source. For a spatially distributed source the picture is more complex. Here we are dealing with multiple spatially segregated sources of various size and amplitude. Differential recordings simply measure the voltage difference and could yield significant values even in the complete absence of a local signal. The same problem applies to the combined reference electrode (eg. Nunez and Srinivasan, 2005). Using CSD analyses indeed appears ideal but this approach works well only with single dipoles or with dipoles with fixed phase delays. Attempts to localize neocortical gamma oscillations with CSD analysis routinely has not been successful despite several attempts in various cortical regions and species, at least not with 100 μm electrode spacings. Furthermore, our electrodes were not perpendicular to the layers in PFC and in several experiments only tetrodes were used. In addition, we suggest that irregular cytoarchitecture, multiple layers and the lower cell packing density of the neocortex make spatio-temporal summation of membrane currents of coherently active neurons in the extracellular space less effective than in the hippocampus. Thus one may not expect to observe spatially confined current sources/sinks associated with rhythmic intracortical network activity. In contrast, sleep spindles and evoked responses have sizable current

sinks associated with synchronous activation of the thalamic projections to a confined layer IV neurons.

Is the Space-Frequency Structure of gFLs Simply a Consequence of Particular Linear Decomposition?

The conclusion that gamma oscillations are localized in space and frequency was first identified by the unit-unit and unit-LFP spectral analyses. It was confirmed by analysis of the gamma bursts isolated in space, frequency and time. These observations led us to the gFL analysis. For physically meaningful linear decomposition of the data some constraints needed to be imposed. Such factorization is the goal of the linear methods like ICA, nonnegative matrix factorization, factor analysis, etc. The constraint could be, for example, independence of the scores, which we cannot not assume since individual gamma oscillators are likely comodulated. Varimax rotation imposes a constraint of simplicity of the factors (Thorstone 1935, Kaiser 1974), which is related to sparseness, as discussed recently in the literature of blind source separation. This constraint is compatible with the spatial and frequency tuning of gamma oscillations observed by independent methods, as spelled out above. Moreover, nowhere in the method is the contiguity of large loading values in space and frequency imposed, yet such structure is discovered by the method – providing evidence that there is sufficient information in the covariance matrix. Critically, the spatial and frequency tuning of gFL factors closely matched our results of unit-LFP spectral analysis. The exact choice of rotation, even though it is data driven, is not unique, and particular choices we make could affect the outcome. One factor that does affect the outcome is the orthogonality of the eigenvectors emposed by the Varimax rotation. Therefore, on a subset of the data we performed the Promax rotation which relaxes the orthogonality. The majority of salient factors remained, though their numbers decreased. Thus, the observed segregation of gamma oscillators, by frequency in particular, could suffer from excessive splitting. Nevertheless, the orthogonality constraint in our analysis did not lead to false positives in subsequent analyses.

Membrane Potential Analysis

In the analysis of intracellular data, spikes were first removed. To achieve this, an average of the intracellular action potential was computed for each cell and the membrane potential was interpolated around all action potential peaks for the duration of the spike. Integrated gamma power was computed in the 25-55 Hz band as a smoothed rectified filtered Vm. Coherence between hippocampal LFP and the membrane potential or the integrated gamma power in the membrane potential was computed using 3.5 sec windows and 5 tapers. Significance of coherence was tested using jackknife resampling method (Thomson and Chave, 1991). This procedure is necessary in light of strong nonstationarity of power in the theta-band in the membrane potential signal. Coherence was considered significant at $p<0.01$. The phase shift between the intracellular signal and LFP in CA1 pyramidal layer was taken at the frequency of maximal coherence. Since in several cases LFP was recorded in the dentate gyrus (e.g. Figure 6C,D), we adjusted the phase shift values for these cells in the group display (Figure 6E) by the phase shift between the LFP in CA1 pyramidal layer and dentate gyrus (~175^{o};Isomura et al., 2006).

Where does the large variability of the phase shifts between the LFP and Vm come from? There are several possible explanations for such variability in phase shift compared to the relatively well concentrated phase preference of suprathreshold firing of neocortical neurons in behaving animals (Figure 2 G,H). First, difference in the state of the animal in different experiments and depth of anesthesia could cause differential attenuation of synaptic transmission in hippocampo-cortical circuits resulting in differential phase shift. Second, due to spontaneous changes of the membrane potential over the course of a long recording session the degree as well as phase of locking of the membrane potential of neocortical neurons to hippocampal LFP can vary within and between animals. Third, due to the limited sample size of the intracellular experiments, a high degree of variability of preferred phases between Vm and LFP is expected, similar to the highly variable preferred phases of significantly theta modulated prefrontal and parietal neurons in REM sleep and waking (Figure 2).

Supplemental Figures

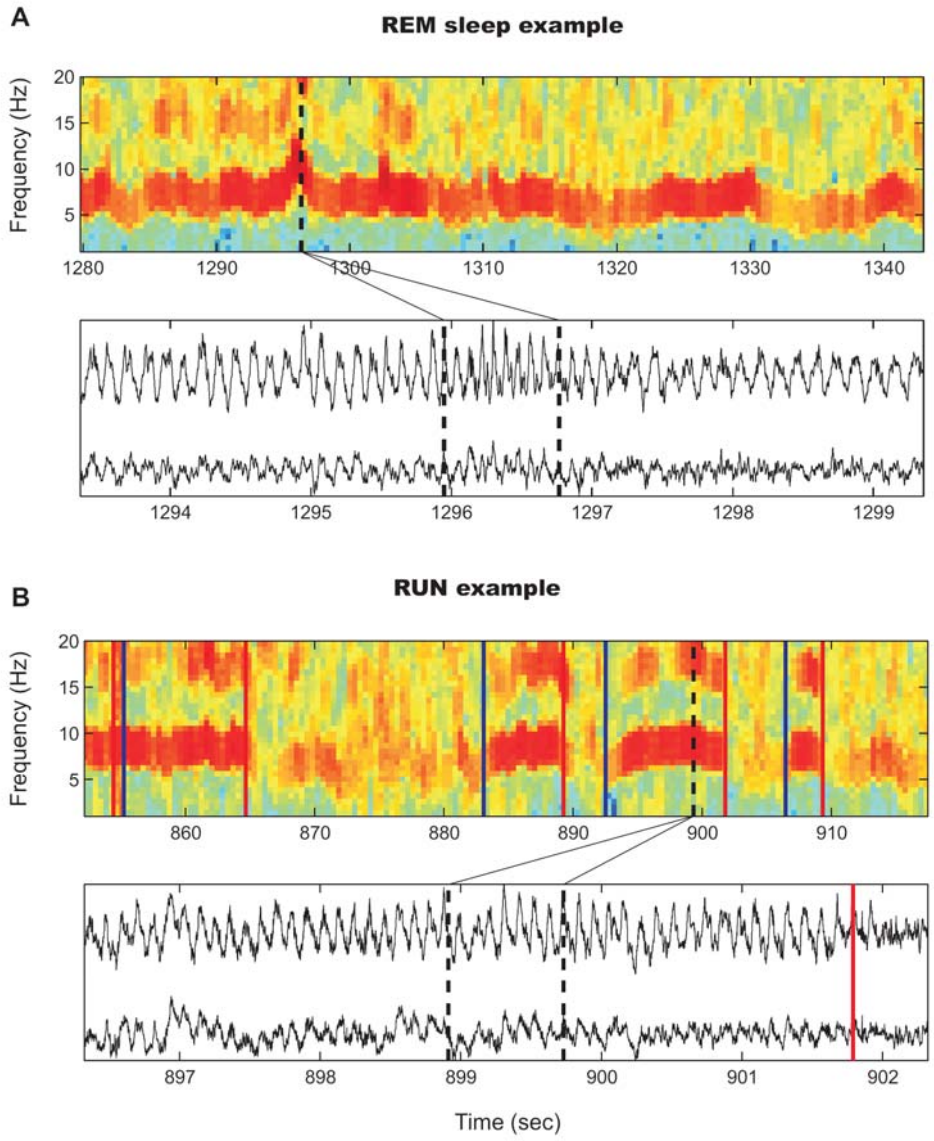

Figure S1. Detection of theta oscillations. Sample spectrograms (top) of LFP recorded in the CA1 pyramidal layer during REM sleep (**A**) and running on an elevated maze (**B**). Traces (bottom plots) display short epochs (dotted lines in spectrograms) of LFP from the CA1 pyramidal layer (top trace) and deep layers of the parietal cortex (bottom trace). Beginning and end of theta episode associated with exploration of the maze is marked by blue and red line, respectively.

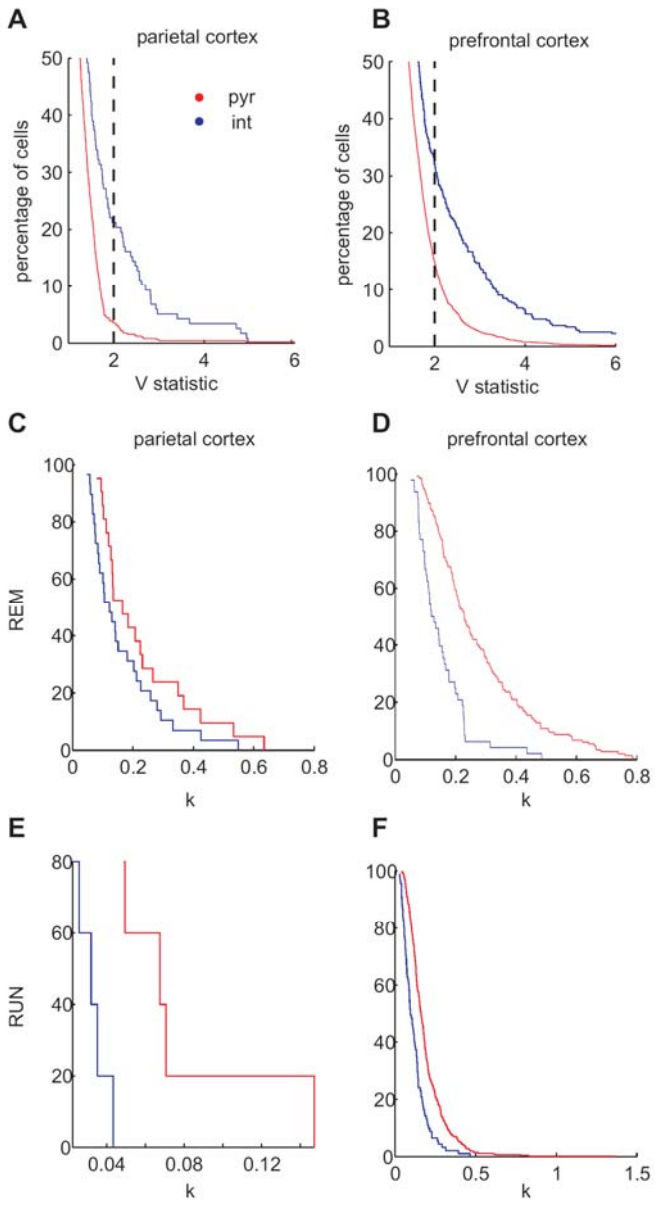

Figure S2. Hippocampal theta modulation of neocortical neurons (additional group statistics). (**A**,**B**) Cumulative density plots for Kuiper test V statistics in parietal (**A**) and prefrontal (PFC, **B**) cortex. Note that there is higher percentage of significantly modulated interneurons than pyramidal cells. The results from nonparametric test against any alternative therefore confirm results of Rayleigh statistics. (**C-F**), Cumulative density plots for ML estimates of concentration parameter *k* for cells with sample size > 1000 for pyramidal cells (red) and interneurons (blue) in parietal (**C,E**) and prefrontal (**D,F**) cortices during REM sleep (**C,D**) and awake running (**E,F**). Note that pyramidal cells invariably have stronger modulation than interneurons. This is in apparent contrast to the finding that a larger percentage of neocortical interneurons is significantly modulated. These observations may be explained by the different features of the two cell types. Interneurons have lower spiking threshold and are more electrotonically compact, thus their output can be shaped by variety of inputs. Pyramidal cells

are constantly inhibited and only the strongly activated ones reach the spiking threshold. Therefore, if both cell types receive comparable periodic subthreshold inputs at theta frequency (signal), their output may reflect different magnitude of non-theta related inputs (noise). As a result, the signal-to-noise ratio of interneurons may be lower than that of pyramidal cells (lower k), yet the large number of spikes emitted by interneurons in a given recording session provides a higher statistical power when tested for theta modulation.

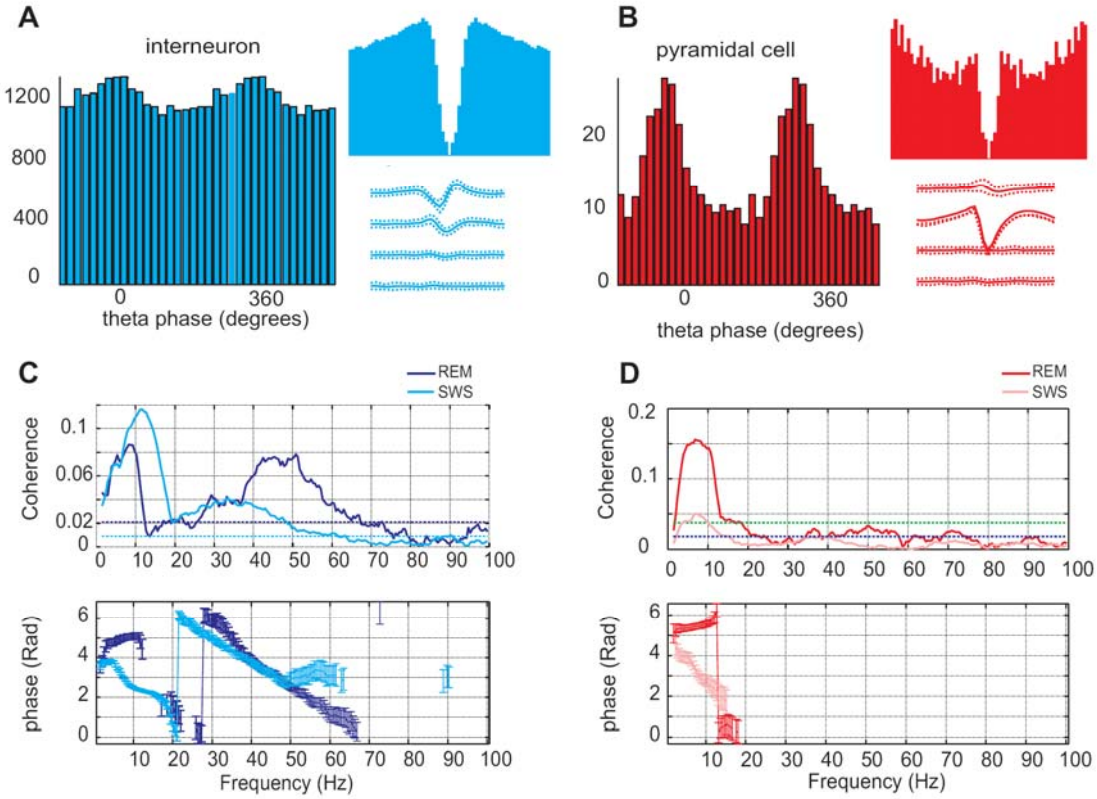

Figure S3. Spectral analysis of theta modulation of neocortical neurons. (**A-D**), Examples of theta modulation of interneuron (A,C, blue) and pyramidal cell (B,D, red). (**A,B**), theta phase histograms (left) and autocorrelograms and spike waveshape (right). (**C,D**), Coherence (top) and phase spectra (bottom) between spike train of respective units and LFP in the neocortex during REM sleep (dark color) and slow waves sleep, SWS (light color). Note peaks in coherence at theta (likely hippocampal theta volume-conducted to neocortex) and gamma frequency during REM sleep and spindle and lower gamma frequencies during SWS. Note linear phase shift with frequency for gamma range (in C, bottom). Such frequency-related phase shift is indicative of a fixed temporal relationship between the mechanisms responsible for gamma LFP and unit firing.

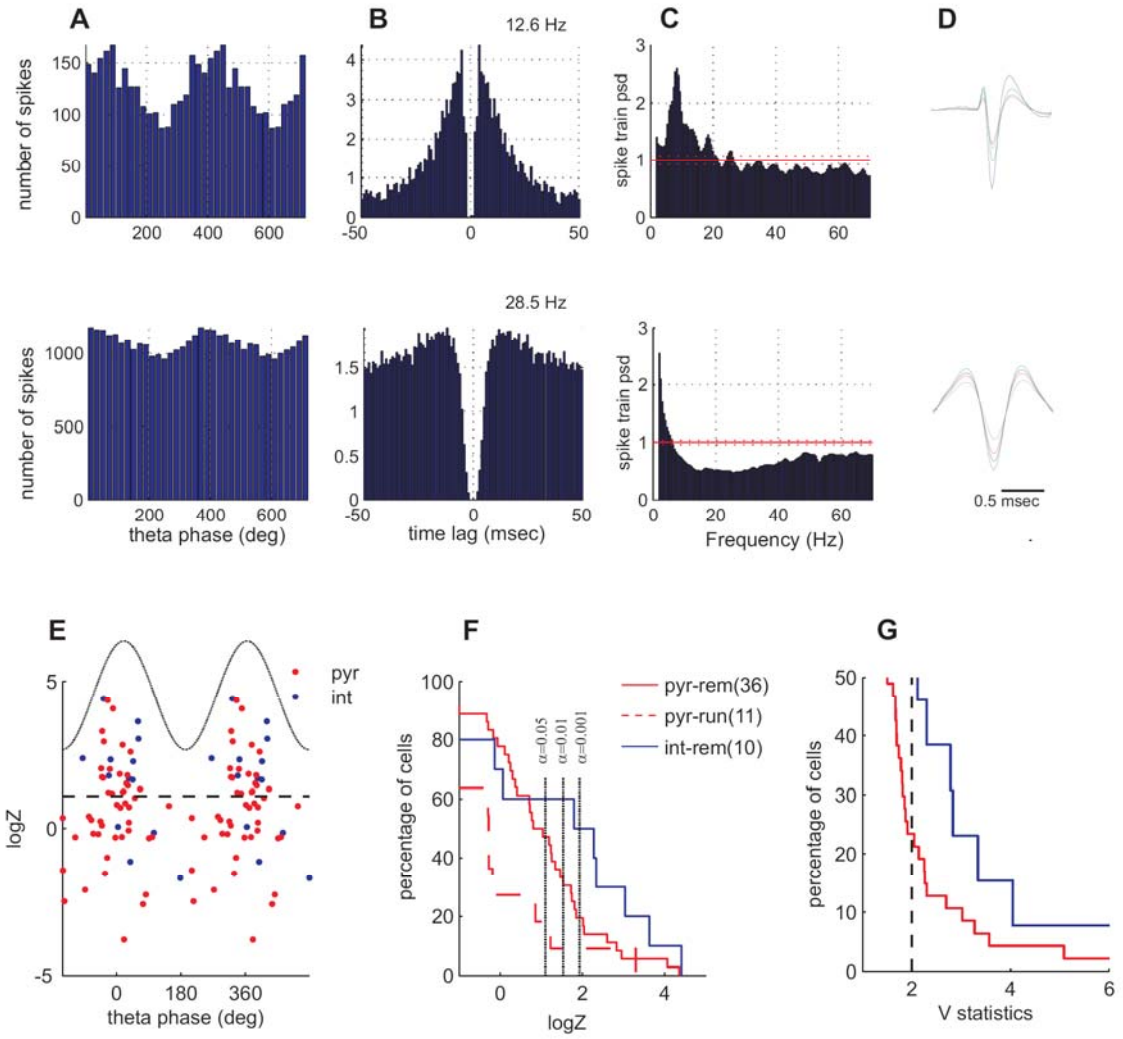

Figure S4. Hippocampal theta oscillation modulates neocortical unit firing in mice. (**A-D**). Two putative interneurons significantly modulated by hippocampal theta. (**A**) Theta phase histograms of neural firing. (**B**) Auto-correlograms of respective neurons. (**C**) Power spectrum of spike trains of respective neurons. Note a distinct spectral peak at theta frequency for the top neuron. Red solid and dotted lines, mean and SD of the power expected for the Poisson process with the same mean rate. (**D**) Average filtered (800 Hz-5 kHz) spike waveshapes of the respective neurons. (**E**) Group data of estimated preferred phase versus Rayleigh statistics (logZ) for all neurons (n=86) in 11 mice. 0, 360^{o}, peak of theta in CA1 pyramidal layer. Dotted line indicates the significance threshold for $p<0.01$. (**F**) Cumulative density function of logZ statistic for putative pyramidal cells and interneurons in different states. (**G**) Cumulative density function of Kuiper V statistic (see Methods) for the same neurons.

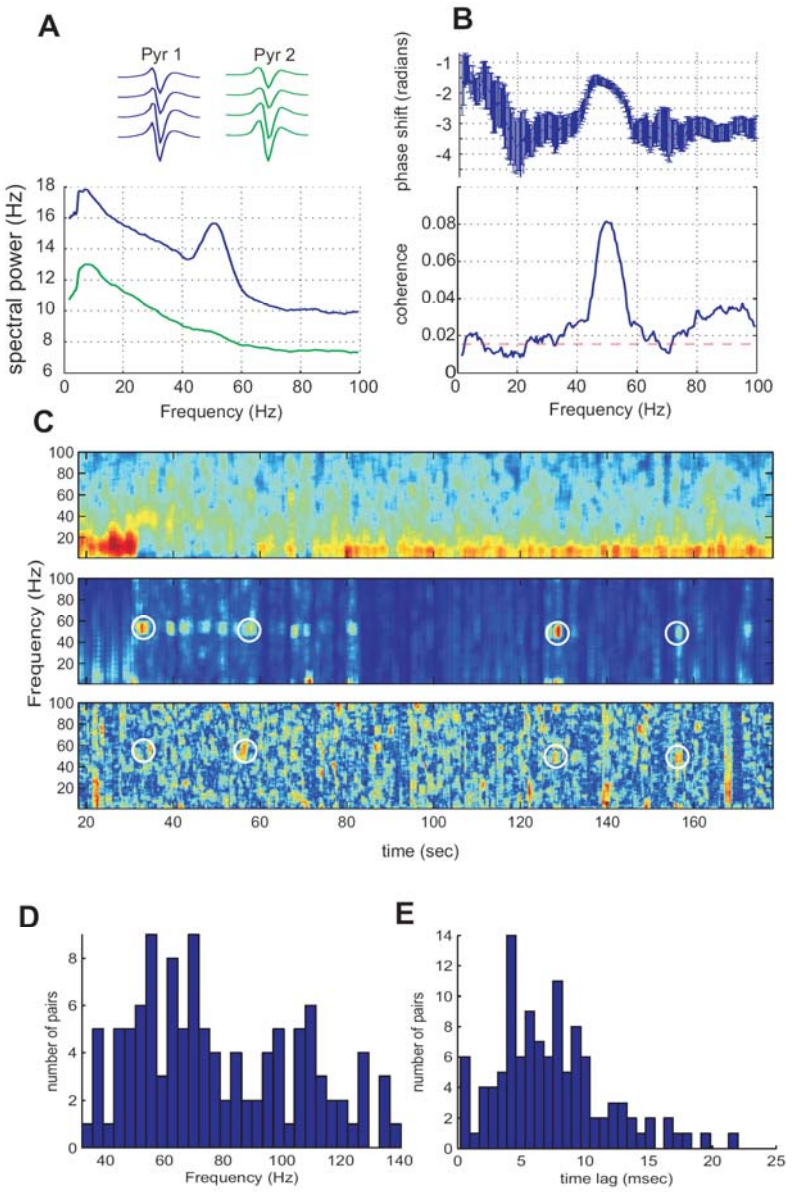

Figure S5. Dynamic gamma synchronization of neocortical neurons. (**A-C**), Example of a pair of putative pyramidal cells synchronized at ~50 Hz gamma frequency. (**A**) Power spectra of spike trains of the two pyramidal neurons. Inset, average filtered spike wave shapes. (**B**) Coherence (bottom) and phase shift (top) between spike trains of the two neurons. (**C**) Sample time stretch of sleep recording illustrating simultaneous time course of the LFP spectrum (top), spectrum of spike train Pyr 1 (middle) and coherence between the two neurons (bottom). Note transient nature of gamma synchronization. The figure illustrates that simple "overall" average spectral measures may not be not adequate to capture gamma frequency coupling between cell pairs or within ensembles of cells. (**D-E**). Group summary of n=113 pairs of neurons, which were significantly coherent in the gamma frequency band. (**D**) Distribution of frequency of gamma synchronization. (**E**) Distribution of time lags between spike trains of gamma-coherent pairs of neurons. Time lags are inferred from the phase shift at the peak gamma frequency.

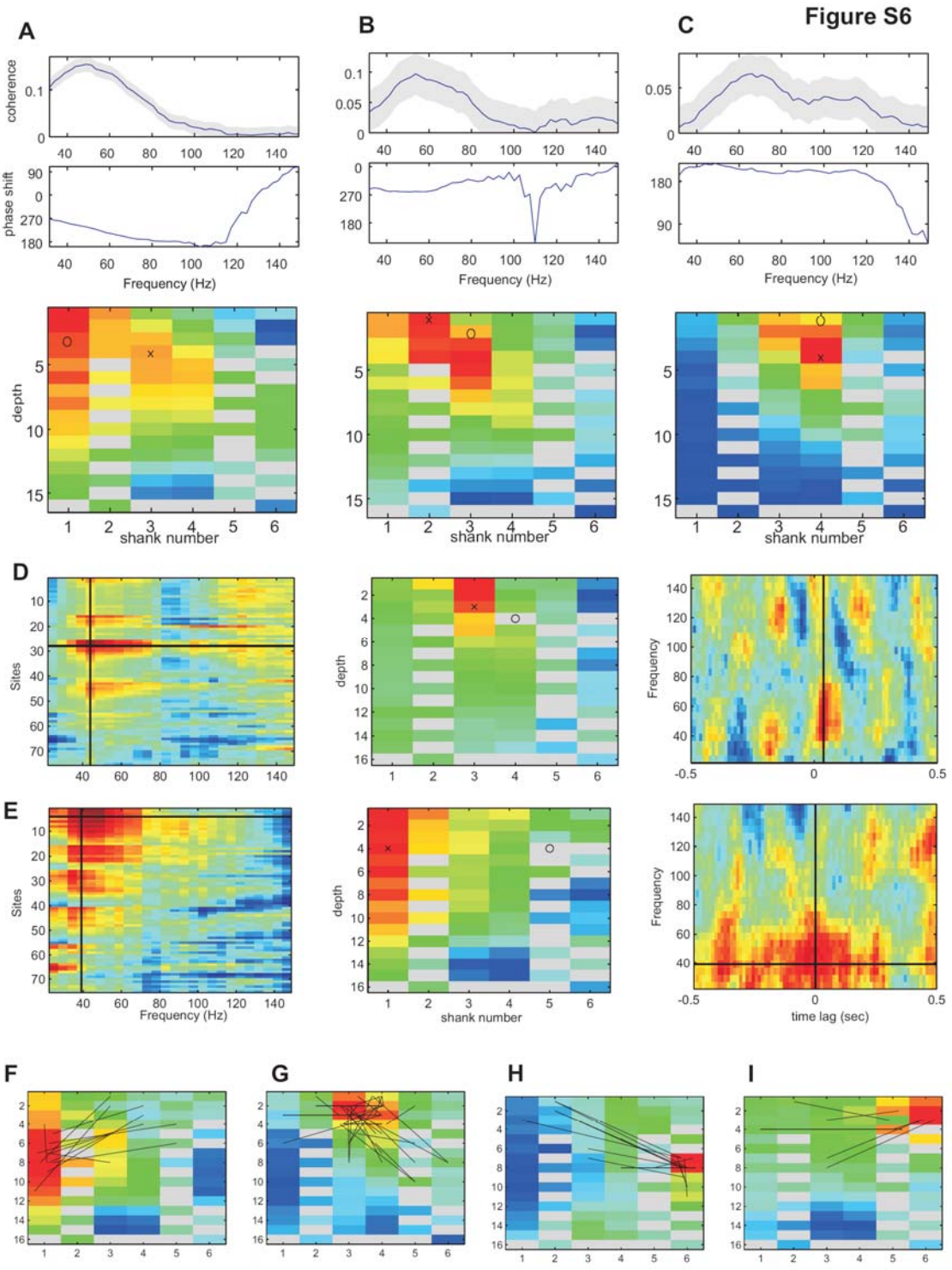

Figure S6. Unit-triggered spectral analysis of gamma oscillations. (A-C), Examples of unit-LFP coherence analysis for different neurons from the same recording session. Top, unit-LFP coherence (gray shading, 95 percentile confidence bands), middle, phase spectrum (0, unit is locked to the peak of the LFP); bottom, anatomical map of spike-LFP coherence at maximal coherence frequency. Circle, putative location of the soma of the unit; cross, site used on the top plots. Note variability of localization in frequency and

anatomical location of the maximal gamma coherence of the LFP to different neurons. (**D,E**), Spike-triggered average spectra for 2 example units. Left panels, deviation of the spike-triggered spectral power from baseline as a function of recording sites (only recording sites without artifacts are shown, y-axis) and frequency (x-axis). Middle panels, anatomical map of spike-triggered spectral power at maximal gamma frequency. Circle, putative cell body location of the unit; cross, site with maximal gamma power. Malfunctioning sites and sites with large amplitude unit spikes (gray) were excluded from the analysis to avoid contamination of gamma power by spike waveshape. Right panels, spike-triggered (time zero) spectral power at the site of maximal gamma power as a function of time lag from the spike. Note similarity in frequency and spatial profiles of the gamma range unit-LFP coherence and unit-triggered spectra. (**F-I**), Average normalized anatomical maps for four anatomical clusters of gamma power profiles triggered by different neurons. Each cluster consists of single unit-triggered profiles with the same or closely overlapping anatomical profile (D,E middle), regardless of gamma frequency. Black lines connect the center of mass of individual unit spike-triggered profiles to the location of the neuron. Note that neuron firing is occasionally best correlated with gamma power increase located as far as 1 mm from the neuron, although most long distance couplings occur in the same cortical layer (putative layer 5, F,G, E).

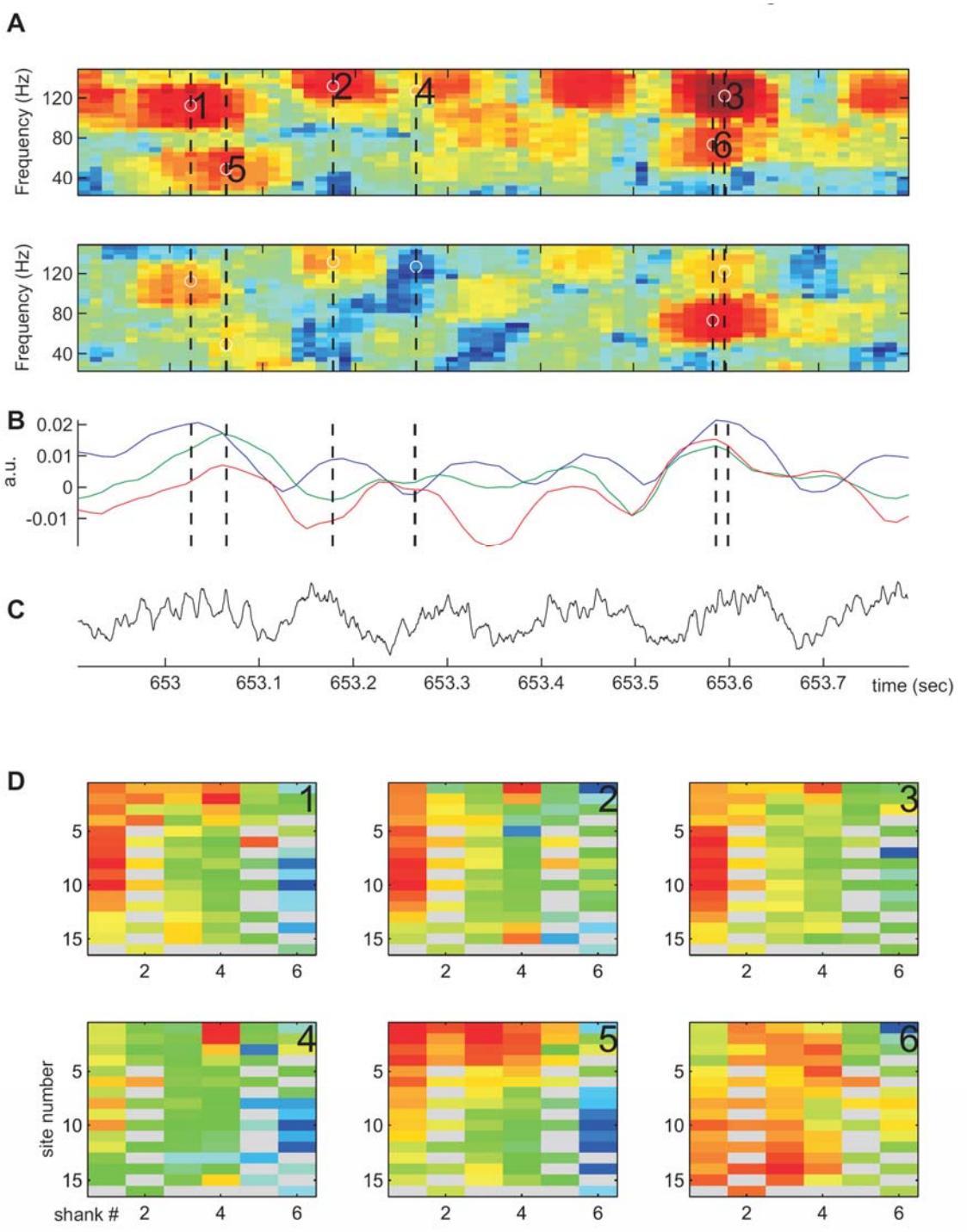

Figure S7. Fine temporal structure of the gFL score signals . (**A**) Sample spectrograms of whitened LFP recorded in neocortical layer 5 (A, top) and hippocampal CA1 pyramidal layer (A, bottom). Dotted lines 1-6 mark time-frequency maxima of spectral power in one of the locations. (**B**) Time course of the 3 gFL scores for the same time period. Blue and green traces correspond to neocortical gFLs and red trace corresponds to hippocampal gFL, whose location-frequency profiles are shown in Figure 5F, 5E and 5H, respectively. Note that times of the peaks of gFL scores closely match the

time of the peaks in the spectrograms (dotted lines 1-3,5 and 6). (**C**) LFP trace recorded in the CA1 pyramidal layer illustrating ongoing theta oscillation. (**D**) Spatial profiles of spectral power at times and frequency bins marked 1-6 in (A). Anatomical layout of recording sites as in Figure 3A. Note that spatial profiles and frequencies at peaks 1-3, 5 and 6 closely correspond to the location-frequency profiles associated with gFLs in Figure 5F, 5E and 5H, respectively. These observations illustrate that peaks in the gFL score exactly correspond to the peaks in spectral power localized in space and frequency according to the respective gFL profile. Note that event 6 corresponds to two gamma oscillations simultaneously present in the hippocampus and neocortex.

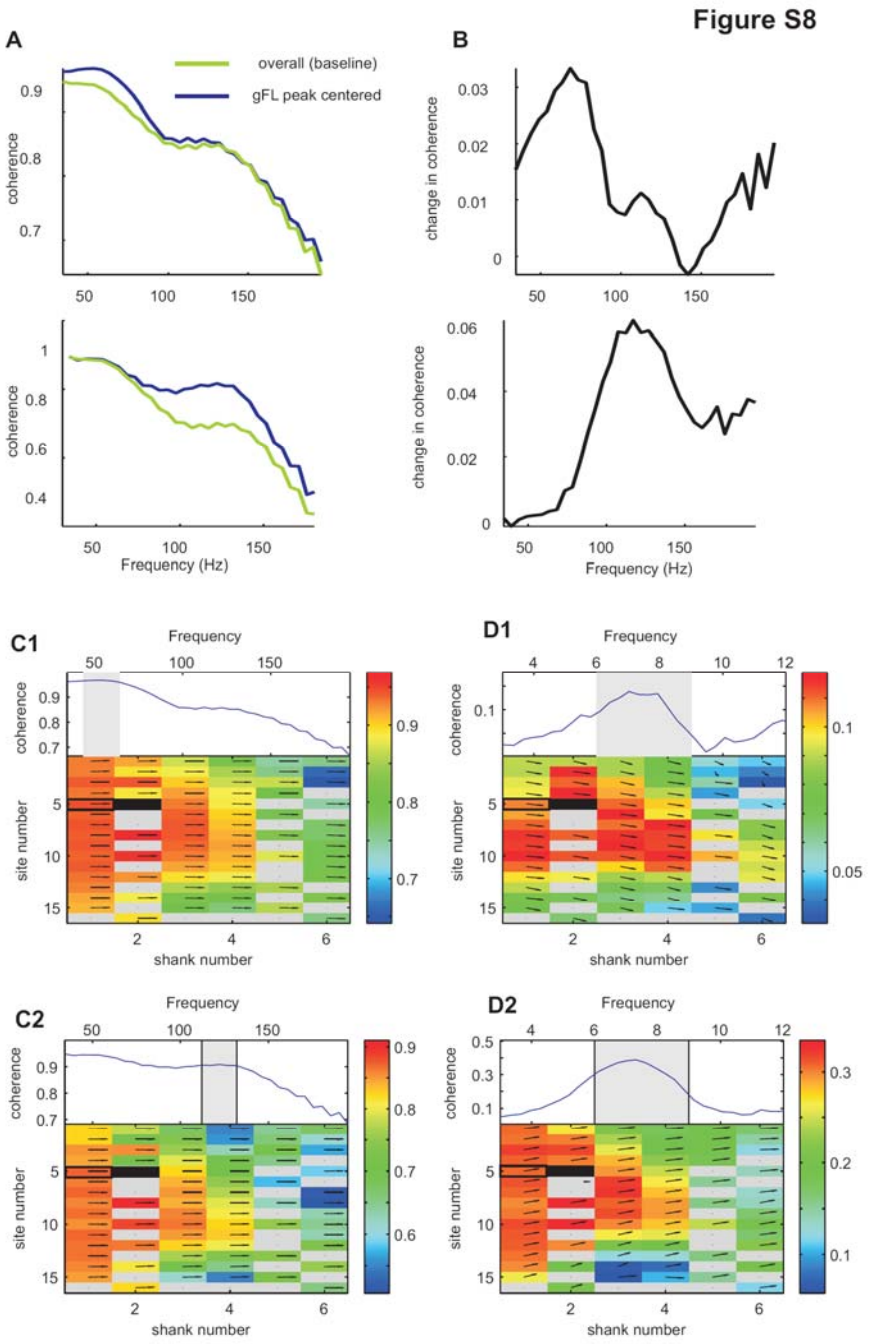

Figure S8. LFP-LFP coherence analysis. (**A**) Example of LFP-LFP coherence between the center of gFL (top #2 Figure 5C and bottom #4 Figure 5D) and a nearby recording site for the entire session (green, baseline) and for spectral windows confined to the time of the peaks of the respective gFL scores (blue). (**B**) The difference between the two coherence spectra in A. Note that peak-confined coherence of gFL score has a frequency-specific increase. (**C,D**) Same display as in Figure 6 J,K for the same gFLs as in A (#2 C1,D1 and #4 C2,D2, respectively). (C1,2) Bottom, spatial map of average coherence between the LFP at the site (solid rectangle) in the center of the respective gFL and other sites at the peak frequency of the gFL profile. Top trace, example coherence for one site

(open rectangle). Arrows, phase shift (zero at 3 o'clock). (D1,2) Top, coherence spectrum between theta LFP and gamma coherence between two neocortical selected sites (theta modulation of coherence). Integrated coherence within the frequency band of maximum coherence was first computed in sliding windows and the coherence between the resulting time series and hippocampal LFP was computed. Bottom, spatial map of theta modulation of coherence between the reference gFL center site and all other sites. Note that the phase shift between hippocampal LFP and neocortical gamma (arrows; 3 o'clock is zero) is different for low and high frequency gamma. This is in agreement with the gFL analysis (Figure 6I), which also showed that the fast gamma is biased to a later phase of theta than low frequency gamma.

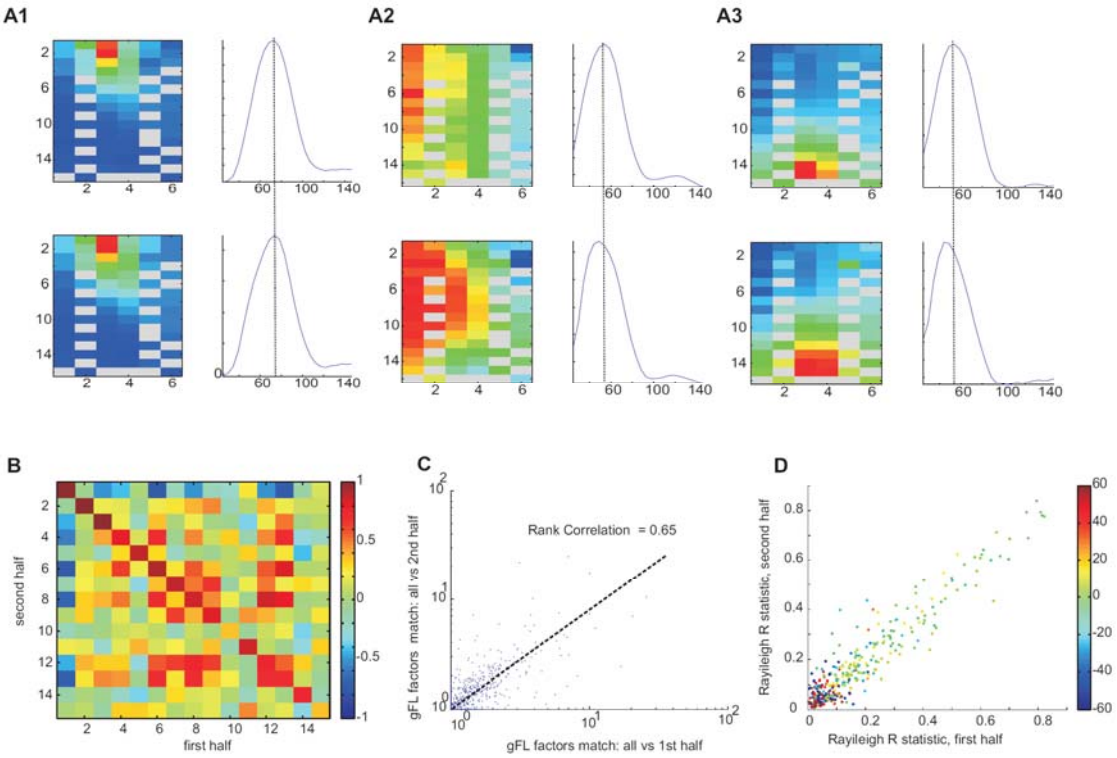

Figure S9. Stability of spatio-temporal features of neocortical gamma oscillations identified by gFL analysis. (**A1-3**) Spatial and frequency profiles of gFLs computed separately from the entire session (top) and first half of the session (bottom). Displays as in Figure 5. (**B**) Rank correlation matrix of aligned gFL factors computed from the first half and second halves of session. Note high values in the diagonal compared to off-diagonal. (**C**) Group data showing the correlation between gFL vector match indexes for the first and second halves. The match index was computed as the ratio of the correlation of the gFL factor in the first (second) half to the closest gFL factor derived from the second half, normalized by the correlation to the next closest gFL from the entire section. Strong correlation between the two halves demonstrates the stability of space-frequency profiles of gamma oscillations and robustness of gFL analysis. (**D**) Rayleigh resultant length (circular measure of concentration of the gFL peaks within the theta cycle) during the first and second halves. Color indicates the phase shift between preferred phases of

gFL peaks within the theta cycle for the two halves of the sessions. Note stability of the theta phase modulation of gFLs within session.

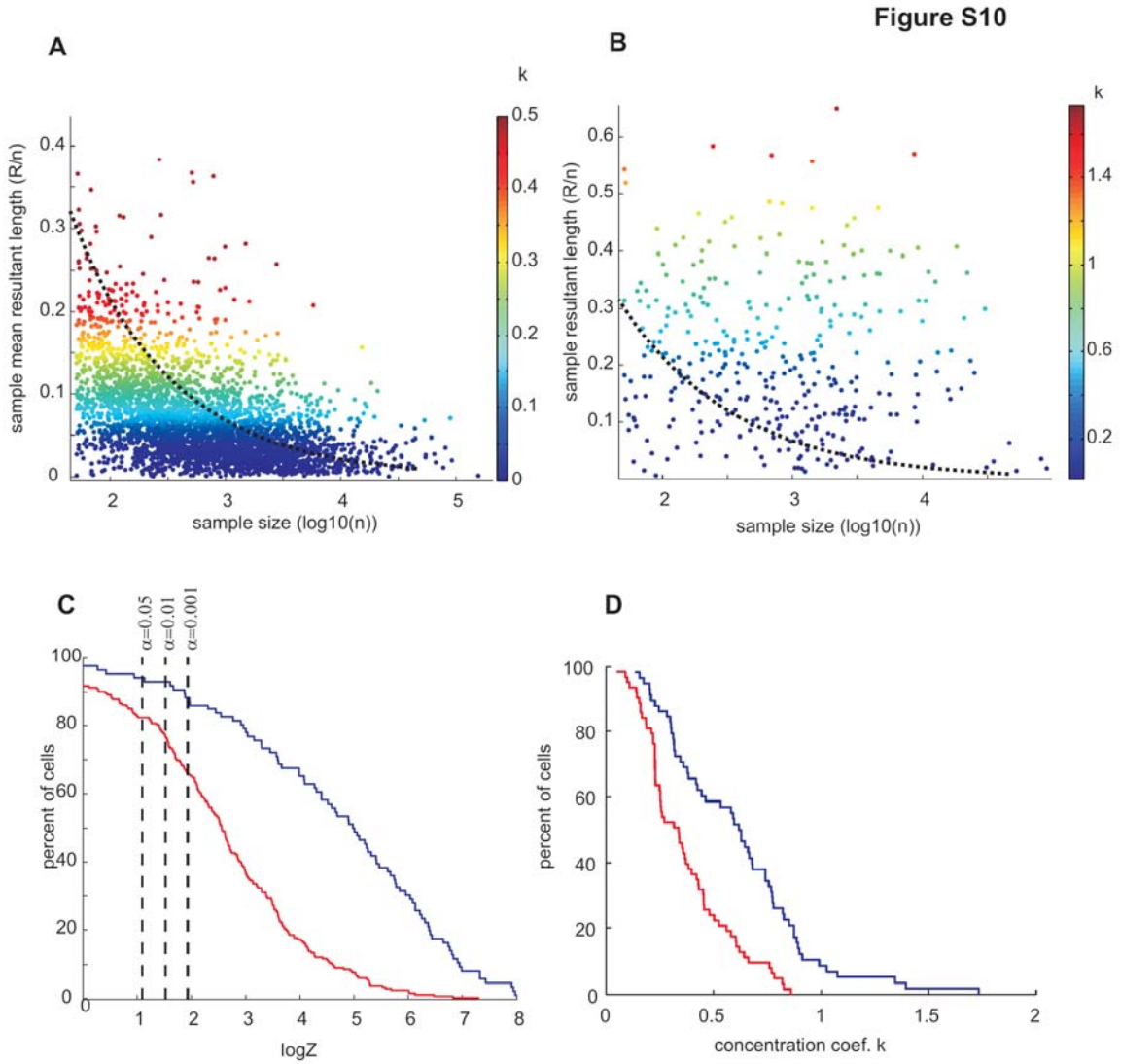

Figure S10. Hippocampal theta phase modulation of hippocampal neurons. (**A,B**) Theta modulation of neocortical (A) and hippocampal neurons (n=349 neurons recorded in CA1, CA3 and dentate regions combined, B). Scatter plots (each dot represents a neuron) of sample resultant length versus sample size (log10 scale) with ML estimate of concentration coefficient *k* color coded. Note difference in color scales. Dots above the dotted line correspond to significantly (at $p<0.01$) theta modulated neurons. Note that density of dots in *R/n-log10(n)* space is virtually uniform in the hippocampus, in contrast to that observed in the neocortex. Most hippocampal cells are significantly modulated compared to the smaller percentage of neocortical cells. (**C**) Percent of neurons (y-axis) with *logZ* statistics greater than given (x-axis, y = P(X>x)). Note that putative interneurons are more likely to be significantly modulated than putative pyramidal cells. Blue, putative interneurons; red, putative pyramidal cells. Vertical dotted lines represent critical values of *logZ* for three levels of significance. (**D**) Percent of significantly

modulated neurons with concentration coefficient *k* greater than given (x-axis, y = P(X>x)). Note that in contrast to the neocortex (Figure S2C-F), hippocampal interneurons are more strongly theta-modulated than pyramidal cells. This may be due to two factors. First, hippocampal pyramidal cells exhibit network dynamics that can accelerate relative to the mean field (Geisler et al., 2007), resulting in a decrease of their concentration coefficient. Second, afferents of most hippocampal interneurons are periodic at theta frequency.

Supplemental References

Bartho,P., Hirase,H., Monconduit,L., Zugaro,M., Harris,K.D., and Buzsaki,G. (2004). Characterization of neocortical principal cells and interneurons by network interactions and extracellular features. J. Neurophysiol. *92*, 600-608.

Bentley,J.J., Lockhart,R.A., and Stephens,M.A. The uniform and von Mises mixture distribution; with applications. 2007. Burnaby, BC, Canada, Department of Statistics and Actuarial Science, Simon Fraser University.
Ref Type: Report

Constantinidis,C., Franowicz,M.N., and Goldman-Rakic,P.S. (2001). Coding specificity in cortical microcircuits: a multiple-electrode analysis of primate prefrontal cortex. J. Neurosci. *21*, 3646-3655.

Csicsvari,J., Henze,D.A., Jamieson,B., Harris,K.D., Sirota,A., Bartho,P., Wise,K.D., and Buzsaki,G. (2003). Massively parallel recording of unit and local field potentials with silicon-based electrodes. J. Neurophysiol. *90*, 1314-1323.

Csicsvari,J., Hirase,H., Czurko,A., and Buzsaki,G. (1998). Reliability and state dependence of pyramidal cell-interneuron synapses in the hippocampus: an ensemble approach in the behaving rat. Neuron *21*, 179-189.

Csicsvari,J., Hirase,H., Czurko,A., Mamiya,A., and Buzsaki,G. (1999). Oscillatory coupling of hippocampal pyramidal cells and interneurons in the behaving Rat. J. Neurosci. *19*, 274-287.

Freeman,J.A., and Nicholson,C. (1975). Experimental optimization of current source-density technique for anuran cerebellum. J. Neurophysiol. *38*, 369-382.

Fujisawa,S., Amarasingham, A., and Buzsaki,G. (2008). Behavior-dependent short-term assembly dynamics in the medial prefrontal cortex. Nat. Neurosci. *11:823-833*.

Geisler,C., Robbe,D., Zugaro,M., Sirota,A., and Buzsaki,G. (2007). ippocampal place cell assemblies are speed-controlled oscillators. Proc. Natl. Acad. Sci. U. S. A *104*, 8149-8154.

Harris,K.D., Henze,D.A., Csicsvari,J., Hirase,H., and Buzsaki,G. (2000). Accuracy of tetrode spike separation as determined by simultaneous intracellular and extracellular measurements. J. Neurophysiol. *84*, 401-414.

Hazan,L., Zugaro,M., and Buzsaki,G. (2006). Klusters, NeuroScope, NDManager: A free software suite for neurophysiological data processing and visualization. J. Neurosci. Methods *155*, 207-216.

Henze,D.A., Borhegyi,Z., Csicsvari,J., Mamiya,A., Harris,K.D., and Buzsaki,G. (2000). Intracellular features predicted by extracellular recordings in the hippocampus in vivo. J. Neurophysiol. *84*, 390-400.

Isomura,Y., Sirota,A., Ozen,S., Montgomery,S., Mizuseki,K., Henze,D.A., and Buzsaki,G. (2006). Integration and segregation of activity in entorhinal-hippocampal subregions by neocortical slow oscillations. Neuron *52*, 871-882.

Jammalamadaka,S.R., and SenGupta,A. (2001). Topics in circular statistics World Scientific).

Jarvis,M.R., and Mitra,P.P. (2001). Sampling properties of the spectrum and coherency of sequences of action potentials. Neural Comput. *13*, 717-749.

Kayser,J., and Tenke,C.E. (2003). Optimizing PCA methodology for ERP component identification and measurement: theoretical rationale and empirical evaluation. Clin. Neurophysiol. *114*, 2307-2325.

Mardia,K.V., and Jupp,P.E. (2000). Directional statistics John Wiley and Sons).

Markram,H. (2006). The blue brain project. Nat. Rev. Neurosci. *7*, 153-160.

Montgomery,S.M., and Buzsaki,G. (2007). Gamma oscillations dynamically couple hippocampal CA3 and CA1 regions during memory task performance. Proc. Natl. Acad. Sci. U. S. A *104*, 14495-14500.

Reyment,R., and Joreskog,K.G. (1993). Applied Factor Analysis in the Natural Sciences Cambridge University Press).

Schou,G. Estimation of the concentration paramter in von Mises-Fisher distributions. Biometrika 65, 369-377. 1978.

Siapas,A.G., Lubenov,E.V., and Wilson,M.A. (2005). Prefrontal phase locking to hippocampal theta oscillations. Neuron *46*, 141-151.

Sirota,A., Csicsvari,J., Buhl,D., and Buzsaki,G. (2003). Communication between neocortex and hippocampus during sleep in rodents. Proc. Natl. Acad. Sci. U. S. A *100*, 2065-2069.

Somogyi,P., Tamas,G., Lujan,R., and Buhl,E.H. (1998). Salient features of synaptic organisation in the cerebral cortex. Brain Res Brain Res Rev *26*, 113-35.

Thomson,D.J., and Chave,A.D. (1991). Jackknifed error estimates for spectra, coherences and transfer functions. S. Haykin, ed. Prentice Hall).

Zugaro,M.B., Monconduit,L., and Buzsaki,G. (2005). Spike phase precession persists after transient intrahippocampal perturbation. Nat. Neurosci. *8*, 67-71.